Title

A framework for target discovery in rare cancers

Authors

Bingchen Li[1,‡], Ananthan Sadagopan[1,‡], Jiao Li[1], Yuqianxun Wu[1], Yantong Cui[1], Prathyusha Konda[1], Cary N. Weiss[1,2], Toni K. Choueiri[1,3,4], John G. Doench[5], Srinivas R. Viswanathan[1,3,4,5*]

Affiliations

[1]Department of Medical Oncology, Dana-Farber Cancer Institute; Boston, MA 02215, USA.

[2]Department of Pediatric Oncology, Dana-Farber Cancer Institute; Boston, MA 02215, USA.

[3]Department of Medicine, Harvard Medical School; Boston, MA 02215, USA.

[4]Department of Medicine, Brigham and Women's Hospital; Boston, MA 02215, USA.

[5]Broad Institute of MIT and Harvard; Cambridge, MA 02142, USA.

‡Authors contributed equally.

*To whom correspondence should be addressed: srinivas.viswanathan@dfci.harvard.edu (S.R.V)

Abstract

While large-scale functional genetic screens have uncovered numerous cancer dependencies, rare cancers are poorly represented in such efforts and the landscape of dependencies in many rare cancers remains obscure. We performed genome-scale CRISPR knockout screens in an exemplar rare cancer, *TFE3*-translocation renal cell carcinoma (tRCC), revealing previously unknown tRCC-selective dependencies in pathways related to mitochondrial biogenesis, oxidative metabolism, and kidney lineage specification. To generalize to other rare cancers in which experimental models may not be readily available, we employed machine learning to infer gene dependencies in a tumor or cell line based on its transcriptional profile. By applying dependency prediction to alveolar soft part sarcoma (ASPS), a distinct rare cancer also driven by *TFE3* translocations, we discovered and validated that *MCL1* represents a dependency in ASPS but not tRCC. Finally, we applied our model to predict gene dependencies in tumors from the TCGA (11,373 tumors; 28 lineages) and multiple additional rare cancers (958 tumors across 16 types, including 13 distinct subtypes of kidney cancer), nominating potentially actionable vulnerabilities in several poorly-characterized cancer types. Our results couple unbiased functional genetic screening with a predictive model to establish a landscape of candidate vulnerabilities across cancers, including several rare cancers currently lacking in potential targets.

Main Text

Introduction

A cornerstone of precision oncology is the matching of therapies to specific cancers based on predictive molecular features. Recent advances in the molecular classification of cancer coupled with advances in genome-scale functional genetic screening have enabled the discovery of multiple biomarker-drug pairs that have proven clinically effective in specific cancer subtypes (1–9). Still, limited molecular profiles of rare cancer types and a paucity of robust cellular models for many of these cancers remain barriers to fully realizing the ideal of precision oncology; this is in spite of the fact that many rare cancers have homogeneous genomic landscapes with singular driver alterations that may be directly linked to robust vulnerabilities (10–12).

Kidney cancer is notable in this regard as it comprises dozens of biologically distinct histologies in both adults and children, many of which are quite rare (13). To date, most discovery biology efforts in kidney cancer have focused on clear-cell renal cell carcinoma (ccRCC), which comprises 75% of RCC in adults and is typified by loss of the *VHL* tumor suppressor gene, leading to activation of hypoxia signaling (14). While therapeutic agents targeting this pathway have demonstrated promise in ccRCC (15), other RCC subtypes do not typically harbor *VHL* alterations and are driven by distinct biology (16). It is therefore likely that subtypes of kidney cancer differ in their dependency profiles, though this has not yet been systematically explored.

Translocation renal cell carcinoma (tRCC) is one such subtype of RCC that strikes both adults and children. Molecularly, tRCC is driven by an activating gene fusion involving an MiT/TFE family transcription factor, most commonly *TFE3* (17). Due to a lack of therapies specifically targeted to the biology of tRCC, therapies for ccRCC are frequently used; however, these yield poor response rates (18–23). The discovery of novel molecular targets in tRCC is therefore a pressing unmet need.

Recent studies have revealed few recurrent genomic alterations in tRCC apart from the driver fusion (23–28). Unbiased functional genetic screening can be useful for nominating vulnerabilities in such cases (11,12), but tRCC cell line models have not yet been included in large scale screening efforts (7,29–31), and only a limited number of cell line models of this cancer have been reported (17,32–34). In addition, *TFE3* fusions can drive a spectrum of other rare cancers apart from tRCC, including alveolar soft part sarcoma (ASPS) (35), perivascular epithelioid cell tumor (PEComa) (36), epithelioid haemangioendothelioma (EHE (37), malignant chondroid syringoma (38), and ossifying fibromyxoid tumors (39). It remains unknown whether these tumor types, most of which do not have models amenable to large-scale screening, have distinct dependency

profiles from tRCC despite sharing the same driver fusion. More broadly, many subtypes of kidney cancer apart from ccRCC have limited cellular or *in vivo* models and have been poorly characterized with respect to their molecular features and dependency landscapes.

In this study, we leveraged genome-scale CRISPR screening to discover selective vulnerabilities in tRCC cell line models. To complement this functional data, we applied a machine learning approach to nominate genetic dependencies based on tumor or cell line transcriptome profiles without the need for functional screening. By applying our predictive modeling to a broad range of tumor and cell line RNA-Seq datasets, with a focus on cancers not evaluated or underrepresented in prior functional screening efforts, we present a landscape of candidate vulnerabilities across multiple different *TFE3* fusion cancers, as well as across 13 different molecular subtypes of kidney cancer.

Results

Genome-scale CRISPR knockout screening of tRCC cells

We performed genome-scale pooled CRISPR-Cas9 knockout screening in three tRCC cell lines representing two distinct *TFE3* fusions (FUUR-1: *ASPSCR1-TFE3*; S-TFE: *ASPSCR1-TFE3*; UOK109: *NONO-TFE3*). Each cell line was stably transduced with Cas9 and subsequently transduced with a lentiviral library of 76,441 single-guide RNAs (sgRNAs) targeting 19,114 genes (Broad Brunello library (40)) with 1,000 non-targeting control sgRNAs. Cells were cultured for 28 days, at which point genomic DNA was extracted and sgRNA abundance was compared to the starting pool; sgRNAs depleted from the pool at the conclusion relative to the start of the experiment were inferred to target tRCC-essential genes (**Fig.1A**).

While the Cancer Dependency Map (DepMap) has profiled >1100 cancer cell lines across 28 lineages via genome-scale genetic (RNAi/CRISPR) screening, tRCC cell lines have to date not been included in this effort (30,41). We therefore sought to calibrate our results against published results from the DepMap in order to identify candidate vulnerabilities that are selectively essential in tRCC relative to other cancer types. For each gene assayed in our screens, we calculated a Chronos score, which represents the relative essentiality of a gene accounting for various potential confounders, including sgRNA efficiency, copy number related bias, and heterogenous cutting events (**Methods**) (31); by the Chronos metric, cell-essential genes have a score of approximately -1 while non-essential genes have a score of approximately 0 (31). We compared Chronos scores for each gene in tRCC cells (averaged across the 3 tRCC cell lines screened in our study) to Chronos scores for these same genes in either clear-cell renal cell carcinoma (ccRCC) cell lines (averaged across 14 cell lines) or all cancer lineages (averaged across 1193 cell lines representing 28 lineages, ccRCC excluded) screened in the DepMap (**Fig.1B-C, Supplementary Table S1, Methods**).

Using established lists of essential and non-essential genes(42), we found that essential genes (reported in DepMap) had a mean Chronos score of –0.930 across tRCC cell lines screened in our study, while non-essential genes had a mean Chronos score of -0.026. Importantly, while cell lines in the DepMap effort were screened using the Avana CRISPR knockout sgRNA library (74,687 sgRNAs targeting ~18,560 genes) (40) and the tRCC cell lines in this study utilized the Brunello library, the strong concordance in the scores for both essential and non-essential genes suggests that informative comparisons can be made between our data and those generated via the DepMap effort, despite the use of different genome-scale sgRNA libraries and the screens being conducted over different durations (43).

Among the most selective dependencies in tRCC cells were *TFE3* and *ASPSCR1* (fusion partner of *TFE3* in two of three cell lines screened) (**Fig.1B-C**). *TFE3* fusions typically retain the C-terminal exons of *TFE3* and the N-terminal exons of the fusion partner (23,44). As the Brunello sgRNA library contains 4 sgRNAs per gene, distributed across the gene body, we next sought to determine the log fold-change of individual sgRNAs in each of our CRISPR knockout screens. We found that sgRNAs targeting C-terminal exons of *TFE3* retained within the oncogenic fusion (E, F, G) were strongly depleted in our screens while an sgRNA targeting exon 4

(not contained within the oncogenic fusion, H) was not. Similarly, sgRNAs targeting N-terminal exons of the *ASPSCR1* or *NONO* fusion partners were strongly depleted in cell lines containing the *ASPSCR1-TFE3* (s-TFE, FU-UR-1) or *NONO-TFE3* fusions (UOK109), respectively. However, depletion of *NONO* sgRNAs was not observed in s-TFE or FU-UR-1 cells, nor was depletion of *ASPSCR1* sgRNAs observed in UOK109 cells (**Fig.1D**, **Supplementary Fig. S1A)**. We conclude that *TFE3* scores as a strongly selective dependency in tRCC lines due to CRISPR-mediated depletion of the oncogenic driver fusion.

To further validate these findings, we performed growth competition assays in tRCC or ccRCC cell lines transduced with Cas9 and either a control sgRNA or an sgRNA targeting *TFE3* (C-terminal region). Strong depletion of *TFE3* knockout cells was observed in all *TFE3*-fusion tRCC cell lines, but not in ccRCC cell lines that express wild type TFE3 (786-O, Caki-1) (**Fig.1E, Supplementary Table S2**). Together, these results indicate that the driver *TFE3* fusion represents the primary selective essentiality in tRCC and that wild type *TFE3* is dispensable in non-fusion cancer cells.

Selectively essential pathways in tRCC

We next sought to discover pathways that might represent selective essentialities in tRCC, beyond the fusion itself. We performed gene ontology enrichment (45) on dependencies selectively essential to tRCC cell lines (defined as ΔChronos ≤ -0.5 between every screened tRCC cell line and either ccRCC cell lines or all lineages in DepMap, **Methods, Supplementary Table S1**). Remarkably, pathways related to oxidative phosphorylation and mitochondrial metabolism were strongly enriched amongst tRCC-selective dependencies (**Fig.2A**, **Supplementary Fig. S1B-C**), and multiple members of biochemical complexes involved in these processes scored as strong selective dependencies in tRCC cells (**Fig.2B-D**). These included: **(1)** genes involved in the transcription and translation of mitochondrially-encoded genes (*POLRMT*: mitochondrial RNA Polymerase that transcribes mitochondrial DNA (mtDNA); *MRPL48*: component of the mitochondrial ribosome ("mitoribosome"); *ERAL1*: involved in mitochondrial rRNA assembly; *NARS2*: mitochondrial asparaginyl tRNA synthetase); **(2)** genes encoding enzymes in the citric acid (TCA) cycle (*SDHA, SDHB*); **(3)** genes encoding components of the mitochondrial ATP synthase and electron transport chain (*ATP5F1A, ATP5F1D, ATP5F1E, ATP5ME, ATP5PD, CYCS*); **(4)** genes involved in the assembly or biogenesis of iron-sulfur clusters, which are critical for Complex I, II and III activity within the electron transport chain (46)(*FDX2, HSCB, ISCA1*) (**Fig.2B, E**). Consistent with this screening data, we functionally validated that knockout of several of these genes (*ISCA1, SDHA*, *MRPL48, POLRMT*) selectively impairs the growth of tRCC cells in assays for cell proliferation, cell viability, and clonogenic capacity (**Fig.2F**, **Supplementary Fig. S2A-D)**. Altogether, these results strongly validate our recent finding that *TFE3* fusions rewire tRCCs toward oxidative phosphorylation, as opposed to the highly glycolytic metabolism of other kidney cancers (47).

Kidney lineage-defining transcription factors (*PAX8*, *HNF1B*) were also strong dependencies in tRCC, as they are in ccRCC **(Fig.1C, Supplementary Fig. S1D)**. PAX8 is a transcription factor in the paired box family that is critical for kidney organogenesis and is broadly expressed in renal epithelial cells as well as in renal parietal cells (48). HNF1B is a homeodomain-containing transcription factor that also plays an important role in nephron development; mutations in this gene represent the most common monogenic cause of developmental renal disease (49). Consistent with these genes being lineage dependencies, knockout of *HNF1B* and *PAX8* was selectively essential to both tRCC and ccRCC cell lines, as previously reported in ccRCC (50), but had no effect on cancer cell lines of other lineages (**Supplementary Fig. S2F-K**). Moreover, dependency of both *PAX8* and *HNF1B* correlated strongly with their expression across the DepMap (*HNF1B*: ρ = -0.42, *P*=1.2e-48; *PAX8*: ρ = -0.26, *P*=2.1e-18) and both genes were highly expressed in tRCC and adjacent kidney-normal tissue, but not in other *TFE3*-driven malignancies (melanotic kidney tumors, PEComa, ASPS) that may be of mesenchymal origin (**Supplementary Fig. S2F-G**). Thus, although tRCCs often display mesenchymal features distinct from most ccRCCs (51), these results functionally suggest that the cancer is of a renal epithelial origin. Three genes involved in mevalonate synthesis (*PMVK, MVK, MVD*) were also strong dependencies in tRCC and had variable levels of dependency across ccRCC cell lines (**Fig.2B-C**,

Supplementary Fig. S2E); given prior reports of perturbed cholesterol biosynthesis in ccRCC, this may also represent a form of lineage dependency that holds across various types of kidney cancer (52,53).

Finally, we uncovered additional strong dependencies that were shared in two of the three screened tRCC cell lines, including cell cycle related genes (*CDK4*), genes involved in hypoxia-inducible factor (HIF) signaling (*EGLN1, VHL*), and genes involved in the antioxidant response (*TXNL4B*, *COA5/6*, *CYC1*) (**Supplementary Fig. S1C**). These represent additional candidate vulnerabilities that could prove therapeutically tractable.

Predicting dependencies in tRCC based on transcriptional profile

The relatively small number of tRCC models available for screening coupled with a diversity in *TFE3* fusion partners and in co-occurring genetic alterations raises the possibility that some strong dependencies may hold only in a subset of tRCC cases. We therefore sought to infer the dependency landscape of a cell line or tumor from its transcriptional profile – a principle that could be broadly applicable since there are many more tumors profiled by RNA sequencing (RNA-Seq) than there are cell line models amenable to large-scale screening, for both tRCC and many other rare cancers.

Although it has been suggested that expression profiles may be used to predict vulnerabilities, prior attempts have been applied primarily to cell line models, have had variable performance in tumor samples (53–56), and have not typically been applied with the granularity of cancer subtypes. We sought to establish a machine-learning model to reliably nominate genetic dependencies from cell line models and tumor RNA-Seq data, with a focus on identifying highly predictable dependencies in rare cancer types for which cell line models are not readily available for functional screening. Our pipeline involves merging and normalization of RNA-Seq data from a cell line model or tumor of interest together with reference data (DepMap cell line or TCGA tumor RNA-seq) followed by use of a machine learning model to predict dependencies; we elected to use solely transcriptome profiles for dependency prediction given prior data that expression features have greater predictive power for vulnerabilities than genomic features (54), and to establish the foundation for a streamlined workflow that could be clinically translated (**Fig.3A, Methods**).

We first assessed our method on the DepMap dataset; we applied 5-fold cross-validation during the train-test cycle using RNA-Seq expression features from each cell line to calculate a predicted Chronos score for each gene. We elected to limit our predictions to highly predictable gene dependencies (defined as $R \geq 0.4$ for predicted vs. experimentally observed Chronos score, averaged across the 5 evaluation folds). We found performance to be maximized with a support vector regression (SVR)-based model (RBF kernel) utilizing the 5000 strongest correlated gene expression features for prediction of each dependency. These criteria enabled prediction of dependency scores for 657 genes (hereafter termed predictable dependencies, "PD"). The model was then retrained on the entirety of the DepMap and deployed (**Supplementary Fig. S3A-C, Supplementary Table S3, Methods**).

We applied our model to calculate predicted dependency scores for PD genes in the three tRCC cell lines for which we had obtained a ground truth via genome-scale CRISPR screening in this study (FU-UR-1, s-TFE, UOK109, **Supplementary Table S4**). We observed a strong correlation between predicted and observed Chronos scores amongst the 657 PD genes in all of these cell lines (FU-UR-1: R=0.71, *P*=4.2e-100; s-TFE: R=0.68, *P*=1.6e-86; UOK109: R=0.62, *P*=3.1e-70) (**Fig.3B**). We also predicted dependency scores in a fourth tRCC cell line (UOK146), on which we had been unable to obtain high-quality genome-scale CRISPR screening data owing to technical limitations (**Fig.3C, Supplementary Table S4**).

We nominated selective dependencies in each of these four tRCC cell lines relative to cancer cell lines screened in the DepMap by comparing predicted Chronos scores for PD genes in each cell line to experimentally derived Chronos scores for the same genes in the DepMap. The lineage dependencies *HNF1B* and *PAX8* were prominently identified as selective in all tRCC cell lines, consistent with our screening data in

s-TFE, UOK109, and FU-UR-1, above. Mitochondrial superoxide dismutase (*SOD2*), identified in our screen as a dependency in all cell lines (**Supplementary Table S1**, **Fig.2B**), was also a predicted dependency in two of three screened cell lines (s-TFE, FU-UR-1, and narrowly missed the cutoff in the third, UOK109). In addition, two other cell lines were predicted to be selectively dependent on *MDM2* (UOK109, UOK146), the E3 ubiquitin ligase that negatively regulates the p53 tumor suppressor (57). Furthermore, *NFE2L2* and *SLC33A1* (which is synthetically essential with NRF2 activation (58)) were predicted to be a dependency in FU-UR-1 cells (**Fig.3C**).

We then applied our dependency prediction to tRCC tumors profiled by RNA-Seq in three independent studies (27,28,59) and again compared predicted Chronos scores to experimentally derived Chronos scores in the DepMap. Reassuringly, dependencies predicted in tRCC cell lines were generally also predicted to be selective dependencies in a subset of tRCC tumors, highlighting the applicability of our pipeline across both cell line models and primary tumor data, and suggesting that existing tRCC models faithfully recapitulate dependencies that would be present in tRCC tumors (**Fig.3D, Supplementary Fig. S3D, Supplementary Table S4, Methods**).

We sought to validate predicted *MDM2* dependency in a subset of tRCC cell lines and tumors, given that multiple small molecules targeting MDM2 are currently being clinically evaluated for cancer indications (57). Consistent with our predictions, *MDM2* knockout selectively impaired viability and clonogenic capacity in UOK109 and UOK146 cells but not in the other two tRCC cell lines (**Fig.3e, Supplementary Fig. S4A**). This effect was phenocopied by the small molecule MDM2 inhibitor, milademetan, which has shown activity in Phase I clinical trials (60) (**Fig.3F**). To further investigate the reason for divergent responses to milademetan across our four tRCC cell lines, we analyzed whole-exome sequencing data in these cell lines. We observed *TP53* mutations in s-TFE and FU-UR-1 cells (**Supplementary Fig. S4B**), likely explaining the lack of response to milademetan in these two cell lines. Notably, across 88 tRCC tumors from 3 distinct datasets, selective *MDM2* dependency was predicted in most tumors (82/88 [93.2%] tumors with $\Delta\text{Chronos}_{(\text{Predicted-DepMap Mean})} \leq -0.20$, **Supplementary Fig. S3D**). The higher predicted frequency of MDM2-sensitive tRCC tumors relative to cell lines may reflect the selection for *TP53* inactivation upon prolonged cell culture *in vitro*; by contrast, genomic studies have indicated that tRCC tumors are almost always *TP53* wild-type (23,61,62).

Finally, we applied our dependency prediction to 20 genes previously reported to be altered in tRCC, even if they were not included in our list of 657 PD genes (23,44). This analysis predicted *KMT2D* to be selectively essential in s-TFE cells relative to other tRCC cell lines (**Supplementary Fig. S4C**), which we validated via arrayed CRISPR/Cas9 knockout **(Supplementary Fig. S4D-E)**. Interestingly, *KMT2D* loss has been associated with metabolic rewiring toward glycolytic metabolism (63). We have recently shown tRCC cells to be dependent on OXPHOS and s-TFE cells have a highly OXPHOS-driven metabolic program (47), which may explain their heightened sensitivity to *KMT2D* knockout.

Altogether, these data indicate the ability to predict potentially actionable dependencies from transcriptome profiles of both tRCC cell line models and tumor samples.

MCL1 dependency in alveolar soft part sarcoma

TFE3 fusions drive a spectrum of rare cancers apart from tRCC, including alveolar soft part sarcoma (ASPS), some endothelial hemangioendotheliomas (EHE), and some perivascular epithelioid cell tumors (PEComa) (64–66). While these cancers share *TFE3* driver fusions, they may differ in terms of the cell of origin as well as in co-occurring genetic driver alterations. We therefore sought to determine whether the dependency profile of ASPS differs from that of tRCC. We performed RNA-seq on two ASPS cell lines: ASPS-1 and ASPS-KY, both of which were too slow-growing to be amenable to genome-scale CRISPR screening, and used our method to predict selective dependencies in ASPS relative to tRCC (**Fig.4A-B, Supplementary Table S4**). Similar predictions were performed on published RNA-Seq data from seven ASPS tumors (67). Although the dependency profiles of tRCC and ASPS cell lines were largely concordant (R=0.64), several dependencies were predicted to be selective for ASPS cells versus tRCC, including *MCL1* and *PRKRA*. Conversely, and

consistent with tRCCs being of renal epithelial origin and ASPS being of a mesenchymal origin, the renal lineage dependencies *PAX8* and *HNF1B* were not predicted in ASPS (**Fig.4A-C**, **Supplementary Fig. S3D**).

We also predicted dependencies in PEComa and EHE, two other sarcomas that can be driven by *TFE3* fusions (64,68) and identified vulnerabilities in PD genes that were selective for these malignancies relative to the cell lines experimentally screened in the DepMap, using the procedure described above. Most selective dependencies predicted in these two rare cancers were shared with ASPS (e.g. *FGFR1*, *MCL1*, *PRKAR1A*, *PRKRA*), including the well validated mesenchymal dependency: *GPX4* (69), consistent with all three tumors being sarcomas (**Fig.4C, Supplementary Fig. S5A-C, Supplementary Table S4**).

Targeting of *MCL1* or *PRKRA* by three distinct sgRNAs selectively impaired viability in ASPS cells (ASPS-1 and ASPS-KY) relative to tRCC cells (UOK109, FUUR-1, S-TFE) (**Fig.4D**, **Supplementary Fig. S5D-F**). Similar profiles of differential sensitivity were observed using the clinical-grade MCL1 inhibitor murizatoclax (70) (**Fig.4E**). To gain additional insights into predictors of *MCL1* sensitivity, we identified features predicting *MCL1* dependency in our model across DepMap cell lines; the top predictor was low *BCL2L1* expression (**Fig.4F**). *BCL2L1* encodes the anti-apoptotic factor BCL-xL, which has itself been identified as a dependency in a subset of ccRCC (71). Lower *BCL2L1* expression strongly correlated with greater *MCL1* dependency (ρ=0.50, P=8.2e-71, **Fig.4G**). We further analyzed *BCL2L1* expression in ASPS cell lines/tumors versus tRCC cell lines/tumors and kidney cancer-adjacent normal tissue, when available, and observed substantially lower *BCL2L1* expression in ASPS relative to tRCC and kidney-adjacent normal tissue (**Fig.4H**).

Overall, these analyses highlight the fact that tRCC and ASPS harbor distinct selective vulnerabilities, despite both cancers sharing the same driver fusion; these differences may be linked to a different cell of origin in each tumor.

Predicting dependencies and therapeutic response across cancer types

We next sought to validate our approach across diverse cancer types. We applied our model to predict dependency scores for PD genes for 11,373 tumors representing 33 lineages in The Cancer Genome Atlas (TCGA) (**Supplementary Table S4**). Reassuringly, when clustered (t-distributed Stochastic Neighbor Embedding, t-SNE) on the basis of predicted dependency score, TCGA tumors clustered by lineage together with cell lines experimentally screened in the DepMap (**Supplementary Fig. S6A**). Dependency prediction in the TCGA recovered strong predicted lineage dependencies in the expected patterns, including *SOX10* in melanoma (both cutaneous and uveal) (72,73) and *CTNNB1* in colorectal cancers (74–76) (**Fig.5A)**. Although our model predicts dependency scores based on the top 5000 expression features, relative feature weights may vary widely from gene to gene. In the case of *SOX10* predicted dependency, *SOX10* expression was weighted most heavily, with *CDH19* feature weight being comparable. Notably, *CDH19* is a direct transcriptional target of SOX10 and plays a critical role in neural crest cell development and migration (77). In the case of *CTNNB1*, multiple biologically plausible expression features were linked to β-catenin signaling predicted dependency, including *AXIN2*, *NKD1*, *ASCL2*, and *BMP4* (78–80) (**Fig.5B**). Our modeling also predicted *CDK4* dependency in a subset of cancers across diverse lineages, notably including breast cancer, where CDK4/6 inhibitors are approved but reliable single-gene biomarkers have proven elusive (81). Finally, dependency on glutathione peroxidase 4 (*GPX4*) was predicted to be most pronounced in mesenchymal lineages, consistent with prior studies (69) (**Fig.5A-B**). We conclude that our approach can recover dependencies predicted by outlier expression of one or two genes (e.g. many lineage dependencies) as well as those correlated with more complex expression profiles.

We next sought to infer the dependency profiles of cell line models that have not yet been subjected to unbiased genetic screening. We predicted dependencies in 458 cell lines that were molecularly characterized in the Cancer Cell Line Encyclopedia (CCLE) effort but which have not yet been subjected to genome-scale CRISPR screening in the DepMap (82) **(Supplementary Table S4)**. A subset of these cell lines (restricting to solid tumor lineages with ≥10 cell lines; N=251) were then clustered on the basis of their

predicted dependency profile, together with 833 cell lines experimentally screened in the DepMap (using experimentally-derived dependency scores for the latter lines). Reassuringly, cell lines and tumors with predicted dependency profiles clustered primarily with experimentally screened cell lines of the same lineage (**Fig.5C**, **Supplementary Fig. S6A**). However, there were notable and informative exceptions. For example, one cell line of mucinous ovarian origin (JHOM2B) clustered together with screened cell lines of bowel lineage; this was driven by shared dependencies on Wnt pathway members (*CTNNB1*, *TCF7L2*) (74), the Wnt-regulated colon lineage-defining transcription factor *SOX9* (83), and *KRAS* (76) (**Supplementary Fig. S6B**). Notably, treatment of mucinous ovarian cancer with gastrointestinal-type chemotherapy regimens is preferred and associated with better outcomes compared to gynecologic regimens (84). Kidney cancer cell lines also clustered in distinct groups. While a majority of screened and predicted cell lines of kidney origin clustered together (**Fig.5c**), five kidney cancer cell lines, whose dependency scores were predicted, clustered together with screened rhabdoid-like cell lines from distinct lineages (malignant rhabdoid tumors of the kidney, extrarenal rhabdoid tumors, embryonal rhabdomyosarcoma, atypical teratoid/rhabdoid tumors (ATRT), and small cell ovarian cancers (ovarian rhabdoid tumors)) (**Fig.5C**). This co-clustering was driven by shared dependencies on polycomb repressive complex 2 (PRC2) subunits (*EZH2*, *EED*) (85–89) and transcriptional activator *EP300* (90) (**Supplementary Fig. S6C-D**). This implies that a tumor's dependency profile can vary considerably based on histologic subtype and other factors and may not merely reflect the organ from which it is derived.

Finally, we explored whether our model could inform response to therapeutic agents with defined molecular targets. While drugs targeting the mammalian target of rapamycin (mTOR) pathway are approved and frequently employed in kidney cancer, accurate biomarkers for patient selection have proven elusive (91). Although *MTOR* was not included in the list of 657 PD genes, it was predicted with reasonable accuracy during testing (R = 0.32, averaged from 5-fold cross-validation). We predicted *MTOR* dependency using tumor RNA-Seq data from patients enrolled in the Checkmate 025 study, a Phase 3 study that compared nivolumab (immune checkpoint inhibitor) with everolimus (mTOR inhibitor) in patients with clear cell renal-cell carcinoma (92). Stratifying by predicted *MTOR* dependency score (median dichotomized), high predicted *MTOR* dependency correlated with better overall (P=0.0078) and progression-free survival (P=0.0381) on the everolimus arm but not the nivolumab arm (OS: P=0.0671, PFS: P=0.9641). Moreover, patients in the everolimus arm with high predicted *MTOR* dependency had similar outcomes to those treated with nivolumab (OS: P=0.3575, PFS: P=0.5949), although nivolumab was superior to everolimus in the overall unselected population (OS: P=0.0069, PFS: P=0.0846) (**Fig.5D**, **Supplementary Fig. S6E)**. Dichotomization by predicted *MTOR* dependency score predicted overall survival on the everolimus arm better than dichotomization using any of the other 657 PD genes (**Supplementary Fig. S6F**). *MTOR* dependency prediction was driven by multiple expression features, with the top predictive feature in DepMap (*DENND2D* expression) also being highly ranked in our model (rank 80/5000) (**Supplementary Fig. S6G**).

Together, these results suggest that our approach can be used to both nominate dependencies and inform response to molecularly-targeted therapies across a wide array of tumor types.

A candidate dependency landscape across rare kidney cancers

Having established the tractability of our approach for nominating dependencies across diverse cancer types, we turned our attention to defining the landscape of dependencies across kidney cancers, which comprise a notoriously heterogeneous group of > 40 molecularly distinct subtypes in both adults and children (13). Many of these cancer types have been poorly characterized, are lacking in cell line models amenable to high throughput screening and represent unmet medical needs. We reasoned that dependency prediction could be used to nominate selective dependencies in several of these molecularly-defined entities, in order to better define the spectrum of dependencies across kidney cancer subtypes.

By surveying published studies, we collected RNA-Seq data of 851 tumors across 13 kidney cancer subtypes and used these data to calculate predicted dependency scores for 657 PD genes, as above (**Fig.6A, Supplementary Table S4**). These tumors were then clustered based on dependency profile together with 22 renal cancer cell lines from the DepMap (on which dependency scores were experimentally determined). Group 1 was comprised primarily of ccRCC tumors and most RCC cell lines (which are enriched for clear-cell type (93)), as well as metabolically divergent chRCC (MD-chRCC) tumors. MD-chRCC have been previously described as a distinct, clinically aggressive subset of chRCC with a distinctive hypermethylation pattern and lacking chromosomal losses normally associated with classical chRCC (59). Interestingly, most MD-chRCC tumors demonstrate sarcomatoid differentiation, which may also be seen in a subset of ccRCC tumors (59,94). Group 2 comprised papillary RCC (pRCC type 1 and type 2) as well as a number of diverse entities that have been historically classified as papillary type 2 RCC (95), including CpG island methylator phenotype RCC (CIMP-RCC) and fumarate hydratase (FH)-deficient RCC. Finally, Group 3 consisted of oncocytic tumors, including chRCC and eosinophilic chRCC (**Fig.6B**, **Supplementary Fig. S6H**). Thus, in total, this analysis collapsed 13 distinct subtypes of RCC into three main dependency classes.

We then more carefully interrogated potentially actionable subtype-specific dependencies in kidney cancer. We performed hierarchical clustering of dependency profiles, restricting to 17 genes selective to at least one of the three dependency groups, and including an additional 46 genes with known drug targets. Clustering based on predicted dependency score recapitulated the broad structure observed on t-SNE based clustering above and lent additional insight into specific pairwise comparisons between subtypes (**Fig.6C**). For example, the lineage transcription factors *HNF1B* and *PAX8* were predicted to be very strong dependencies in ccRCC, papillary type 1 and type 2, and most other RCC subtypes with the notable exception of the oncocytic tumors (chRCC, eosinophilic chRCC, oncoytoma, and MD chRCC); this is likely consistent with the former classes of tumors arising from proximal tubule kidney epithelial cells and the latter class arising from mitochondria-rich cells of the distal nephron (96). Notably, *PAX8* and *HNF1B* vary in expression level throughout the nephron, and these gene dependencies are highly correlated to expression level (97,98). Moreover, *HNF1B* is essential for the development of the proximal but not distal tubule(99) (**Fig.6D**, **Supplementary Fig. S2**).

We also observed differential *KEAP1* and *NFE2L2* dependency across RCC subtypes (**Fig.6E**). In particular, FH-deficient RCC and CIMP-RCC were predicted to be strongly dependent on *NFE2L2*, consistent with prior reports of NRF2 pathway activation in these subtypes via methylation of *KEAP1* (CIMP-RCC) or succinylation of *KEAP1* (FH-RCC) (100–102). Although *KEAP1* loss activates NRF2, which is typically oncogenic (103), a subset of RCCs across lineages had predicted dependency scores suggestive of *KEAP1* dependency. This is consistent with recent studies demonstrating that cancers may be sensitive to both oxidative stress (*NFE2L2* dependency) and reductive stress (*KEAP1* dependency), depending on their underlying metabolic features (47,104,105).

Other dependencies appeared to reflect differing rates of genomic alterations across RCC subtypes. For example, *DDX3X* dependency, a paralog dependency known to be unmasked by loss of the Y-chromosome encoded paralog *DDX3Y* (106), was predicted to be among the strongest in pRCC-T1, a tumor type with almost universal somatic loss of the Y chromosome (LOY) (107); accordingly, *DDX3X* dependency was nearly identical between male and female pRCC-T1 samples, but male ccRCC samples (which typically do not show LOY) were far less dependent on *DDX3X,* due to paralog buffering from *DDX3Y* (**Fig.6F**). Most kidney tumors were expected to be dependent on *MDM2*, consistent with the low frequency of *TP53* mutations in this lineage (108); however, *TP53* mutant tumors were predicted to be less *MDM2* dependent than their lineage-matched *TP53* wild-type counterparts (**Supplementary Fig. S6I**).

Dependencies in selenium metabolism (*SEPHS2, SEPSECS, GPX4*), which would be predicted to induce cell death via ferroptosis, were strongest in ccRCC, consistent with prior functional studies in this

subtype (109). MD-chRCC also shared this profile, consistent with most MD-chRCCs displaying a mesenchymal signature associated with ferroptosis sensitivity (59,69). Other RCC subtypes also differed in their predicted dependency on various genes involved in apoptotic cell death (*BCL2*, *MCL1*, *BCL2L1*), with FH-deficient RCC and CIMP-RCC predicted to be particularly dependent on *BCL2L1* and oncocytic tumors more dependent on *BCL2*. By contrast to ASPS, as discussed above, few RCCs showed predicted dependency on *MCL1* (**Fig.6G**). Overall, these analyses suggest subtype differences in vulnerabilities to specific modes of cell death.

Finally, we sought to nominate dependencies in renal tumors with sarcomatoid and/or rhabdoid differentiation (S/R RCCs) (**Supplementary Table S4**); these aggressive features are thought to represent a dedifferentiation event that can occur in renal tumors of diverse parental histologies (94). Despite being clinically aggressive, immune checkpoint inhibitors appear to be particularly effective in S/R RCC for somewhat unclear reasons and additional treatment strategies for this subset of RCC represent an unmet need (94). Using previously annotated S/R RCCs within the TCGA (94), we identified predicted dependencies that were selective to S/R RCCs. Dependencies related to PRMT5 function (*MAT2A* (99) and *WDR77*) were prominently identified as S/R RCC-selective. These likely stem from the established synthetic lethal relationship of *PRMT5* and *MTAP* deletion (110,111); *MTAP* is frequently co-deleted with *CDKN2A,* a deletion event that is strongly enriched in S/R RCCs (23). Additional S/R RCC-selective dependencies include *PPP2CA*, the gene encoding protein phosphatase-PP2A. Notably, PP2A inhibitors have been clinically developed and shown durable anti-tumor activity when combined with immune checkpoint blockade (112,113). Finally, *BCL2L1* dependency is also predicted to be enriched in S/R RCC. *BCL2L1*, which encodes the BCL-xL antiapoptotic protein, has recently been reported as a dependency of mesenchymal kidney cancers; intriguingly, S/R RCCs are known to strongly upregulate epithelial-mesenchymal transition (EMT) programs (**Fig.6H**) (71,94).

Notably, S/R RCCs were derived from all RCC groups, with the majority being derived from group 1 (comprised of ccRCCs and MD-chRCCs) (**Fig.6GG**, **Supplementary Fig. S6J**). This analysis supports the ability to recover candidate dependencies associated with the sarcomatoid differentiation state, rather than only those linked to the lineage from which S/R RCCs are derived. This also suggests that kidney cancers of various histologies may converge on a dependency profile associated with this sarcomatoid/mesenchymal state.

Overall, we provide a landscape of dependencies in rare kidney cancers that could be used as a starting point to develop mechanism-inspired therapeutic strategies in these diseases.

Discussion

In this study, we performed genome-scale CRISPR knockout screening in three cell line models of tRCC, a rare renal tumor not previously included in large scale screening efforts. We identify the *TFE3* fusion as the primary vulnerability in tRCC, consistent with recent genomic studies demonstrating that the fusion represents the dominant, and often sole, driver event in this cancer (23,25–28,44). Given the dispensability *of TFE3* in normal tissues (114) and in all cancer cell lines screened to date in the DepMap, the *TFE3* fusion represents an attractive and highly selective target in tRCC, albeit challenging from the standpoint of druggability.

Our study also reveals additional selective vulnerabilities in tRCC, most notably multiple genes involved in mitochondrial metabolism and oxidative phosphorylation, including components of the citric acid (TCA) cycle, mitochondrial transcription and translation, and the electron transport chain. These unbiased screens dovetail remarkably with our recent study demonstrating that TFE3 fusions metabolically rewire tRCCs towards oxidative phosphorylation (OXPHOS) via transcriptional activation of multiple genes involved in oxidative metabolism and mitochondrial biogenesis (47). They are also consistent with the role of wild type TFE proteins as critical regulators of energy metabolism (115–117). Individual genes within these or related

pathways may represent more tractable therapeutic targets than the fusion itself and may represent inroads to modulate critical downstream pathways driven by TFE3.

However, our tRCC screens also highlight a critical limitation of unbiased functional genomics in rare cancers - namely, the number and availability of suitable models. Over fifteen different *TFE3* fusion partners have been reported (23), but only two distinct fusions were represented in the three cell lines screened in this study. For example, we found the tRCC cell line UOK146, which harbors the relatively common *PRCC-TFE3* fusion (23), to be not technically amenable to genome-scale CRISPR knockout screening. Additionally, while ASPS is also driven by a TFE3-fusion, available ASPS cell lines are slow growing and challenging to culture at the scale required for genome-scale screening. Many other rare adult and pediatric malignancies that would benefit from targeted therapeutics have not been included in unbiased functional screening efforts due to their rarity or due to existing models being unamenable to screening.

We attempted to bridge this gap by pursuing the alternative approach of predicting a tumor's dependency landscape via its transcriptional profile. Recent studies have reported approaches to predict a tumor's dependency profile by virtue of its transcriptional and/or genomic features (54,56,118). While each of these models differs somewhat in approach, all are complementary and formal benchmarking would be required to hone the most accurate method for predicting tumor vulnerabilities. Our approach utilizes predictive expression features that can be readily obtained by clinical transcriptome sequencing of tumor tissue and we suggest that this or a similar approach can be broadly useful to guide treatment selection in rare cancers, for which there is often no evidence-based standard of care. This approach may also be developed to therapies that have a clearly defined molecular target (e.g. everolimus) but no robust biomarker in clinical use.

We predict and validate dependencies across a host of rare cancer types not well-represented in the TCGA and validate several key examples. Via this approach we identified differential dependencies between tRCC and ASPS despite both cancers sharing the same driver fusion, with ASPS cells being selectively sensitive to MCL1 inhibition. Notably, multiple MCL1 inhibitors have advanced clinically; although cardiac toxicity has proven a challenge to earlier agents, newer MCL1 inhibitors appear not to have this liability (119,120). Our study suggests that CDK4/6 inhibitors, EGLN1 inhibitors (47), and MDM2 inhibitors represent additional classes of agents with clinically advanced molecules that could be tested for activity in tRCC or ASPS.

Finally, by applying dependency prediction to a spectrum of kidney cancers, we suggest that kidney cancer subtypes have notably distinct dependency landscapes. Remarkably, although there are several dozen histologic types of kidney cancer, many with multiple expression subtypes (13), we find that kidney cancers collapse into three main groups in dependency space. Intriguingly, S/R RCCs (which can be derived from various RCC subtypes) span multiple dependency clusters and share a small set of unique dependencies. Most discovery biology in kidney cancer has to date has focused on ccRCC: while this has resulted in marked improvements in the treatment of ccRCC over the last decade, these therapies are typically less effective in non-ccRCCs (121), which may be driven by distinct biology. Dependencies related to energy metabolism encapsulate this notion: while deficiency in TCA cycle enzymes such as FH and SDHA/B drives tumorigenesis in glycolytic renal cancers (e.g. FH-RCC and ccRCC), these same genes represent dependencies in high OXPHOS renal cancers such as tRCC (47). We nominate several potentially actionable dependencies, including BCL-xL (*BCL2L1*), *DDX3X*, *MAT2A* and *NFE2L2* that may represent novel therapeutic targets in subsets of kidney cancer.

Overall, we suggest that our combined approach of functional screening and dependency prediction may catalyze precision oncology in many settings, particularly for rare cancers and in many pediatric cancers, where experimental models may be limited, or where discovery biology efforts are resource-limited by small commercial markets and modest industry investment.

References

1. Konda P, Garinet S, Van Allen EM, Viswanathan SR. Genome-guided discovery of cancer therapeutic targets. Cell Reports. 2023;42:112978.

2. Hahn WC, Bader JS, Braun TP, Califano A, Clemons PA, Druker BJ, et al. An expanded universe of cancer targets. Cell. 2021;184:1142–55.

3. Garraway LA, Lander ES. Lessons from the Cancer Genome. Cell. 2013;153:17–37.

4. MacConaill LE, Garraway LA. Clinical Implications of the Cancer Genome. JCO. Wolters Kluwer; 2010;28:5219–28.

5. Basu A, Bodycombe NE, Cheah JH, Price EV, Liu K, Schaefer GI, et al. An interactive resource to identify cancer genetic and lineage dependencies targeted by small molecules. Cell. 2013;154:1151–61.

6. Parrish PCR, Thomas JD, Gabel AM, Kamlapurkar S, Bradley RK, Berger AH. Discovery of synthetic lethal and tumor suppressor paralog pairs in the human genome. Cell Reports. 2021;36:109597.

7. Behan FM, Iorio F, Picco G, Gonçalves E, Beaver CM, Migliardi G, et al. Prioritization of cancer therapeutic targets using CRISPR–Cas9 screens. Nature. 2019;568:511–6.

8. Pacini C, Duncan E, Gonçalves E, Gilbert J, Bhosle S, Horswell S, et al. A comprehensive clinically informed map of dependencies in cancer cells and framework for target prioritization. Cancer Cell. Elsevier; 2024;42:301-316.e9.

9. Viswanathan SR, Nogueira MF, Buss CG, Krill-Burger JM, Wawer MJ, Malolepsza E, et al. Genome-scale analysis identifies paralog lethality as a vulnerability of chromosome 1p loss in cancer. Nat Genet. 2018;50:937–43.

10. Jamshidi F, Nielsen TO, Huntsman DG. Cancer genomics: why rare is valuable. J Mol Med. 2015;93:369–81.

11. Dharia NV, Kugener G, Guenther LM, Malone CF, Durbin AD, Hong AL, et al. A first-generation pediatric cancer dependency map. Nat Genet. Nature Publishing Group; 2021;53:529–38.

12. Sharifnia T, Wawer MJ, Goodale A, Lee Y, Kazachkova M, Dempster JM, et al. Mapping the landscape of genetic dependencies in chordoma. Nat Commun. 2023;14:1933.

13. Moch H, Cubilla AL, Humphrey PA, Reuter VE, Ulbright TM. The 2016 WHO Classification of Tumours of the Urinary System and Male Genital Organs—Part A: Renal, Penile, and Testicular Tumours. European Urology. 2016;70:93–105.

14. Schödel J, Grampp S, Maher ER, Moch H, Ratcliffe PJ, Russo P, et al. Hypoxia, Hypoxia-inducible Transcription Factors, and Renal Cancer. European Urology. 2016;69:646–57.

15. Shirole NH, Kaelin WG. von-Hippel Lindau and Hypoxia-Inducible Factor at the Center of Renal Cell Carcinoma Biology. Hematol Oncol Clin North Am. 2023;37:809–25.

16. John A, Spain L, Hamid AA. Navigating the Current Landscape of Non-Clear Cell Renal Cell Carcinoma: A Review of the Literature. Current Oncology. Multidisciplinary Digital Publishing Institute; 2023;30:923–37.

17. Kauffman EC, Ricketts CJ, Rais-Bahrami S, Yang Y, Merino MJ, Bottaro DP, et al. Molecular genetics and cellular features of TFE3 and TFEB fusion kidney cancers. Nat Rev Urol. 2014;11:465–75.

18. Choueiri TK, Lim ZD, Hirsch MS, Tamboli P, Jonasch E, McDermott DF, et al. Vascular endothelial growth factor-targeted therapy for the treatment of adult metastatic Xp11.2 translocation renal cell carcinoma. Cancer. 2010;116:5219–25.

19. Malouf GG, Camparo P, Oudard S, Schleiermacher G, Theodore C, Rustine A, et al. Targeted agents in metastatic Xp11 translocation/TFE3 gene fusion renal cell carcinoma (RCC): a report from the Juvenile RCC Network. Ann Oncol. 2010;21:1834–8.

20. Boilève A, Carlo MI, Barthélémy P, Oudard S, Borchiellini D, Voss MH, et al. Immune checkpoint inhibitors in MITF family translocation renal cell carcinomas and genetic correlates of exceptional responders. j immunotherapy cancer. 2018;6:159.

21. Chanzá NM, Xie W, Bilen MA, Dzimitrowicz H, Burkart J, Geynisman DM, et al. Cabozantinib in advanced non-clear-cell renal cell carcinoma: a multicentre, retrospective, cohort study. Lancet Oncol. 2019;20:581–90.

22. Alhalabi O, Thouvenin J, Négrier S, Vano Y-A, Campedel L, Hasanov E, et al. Immune Checkpoint Therapy Combinations in Adult Advanced MiT Family Translocation Renal Cell Carcinomas. The Oncologist. 2023;28:433–9.

23. Bakouny Z, Sadagopan A, Ravi P, Metaferia NY, Li J, AbuHammad S, et al. Integrative clinical and molecular characterization of translocation renal cell carcinoma. Cell Rep. 2022;38:110190.

24. Malouf GG, Monzon FA, Couturier J, Molinié V, Escudier B, Camparo P, et al. Genomic heterogeneity of translocation renal cell carcinoma. Clin Cancer Res. 2013;19:4673–84.

25. Malouf GG, Su X, Yao H, Gao J, Xiong L, He Q, et al. Next-generation sequencing of translocation renal cell carcinoma reveals novel RNA splicing partners and frequent mutations of chromatin-remodeling genes. Clin Cancer Res. 2014;20:4129–40.

26. Marcon J, DiNatale RG, Sanchez A, Kotecha RR, Gupta S, Kuo F, et al. Comprehensive Genomic Analysis of Translocation Renal Cell Carcinoma Reveals Copy-Number Variations as Drivers of Disease Progression. Clin Cancer Res. 2020;26:3629–40.

27. Sun G, Chen J, Liang J, Yin X, Zhang M, Yao J, et al. Integrated exome and RNA sequencing of TFE3-translocation renal cell carcinoma. Nat Commun. Nature Publishing Group; 2021;12:5262.

28. Qu Y, Wu X, Anwaier A, Feng J, Xu W, Pei X, et al. Proteogenomic characterization of MiT family translocation renal cell carcinoma. Nat Commun. Nature Publishing Group; 2022;13:7494.

29. Meyers RM, Bryan JG, McFarland JM, Weir BA, Sizemore AE, Xu H, et al. Computational correction of copy number effect improves specificity of CRISPR-Cas9 essentiality screens in cancer cells. Nat Genet. 2017;49:1779–84.

30. Tsherniak A, Vazquez F, Montgomery PG, Weir BA, Kryukov G, Cowley GS, et al. Defining a Cancer Dependency Map. Cell. 2017;170:564-576.e16.

31. Dempster JM, Boyle I, Vazquez F, Root DE, Boehm JS, Hahn WC, et al. Chronos: a cell population dynamics model of CRISPR experiments that improves inference of gene fitness effects. Genome Biol. 2021;22:343.

32. Ishiguro M, Iwasaki H, Ohjimi Y, Kaneko Y. Establishment and characterization of a renal cell carcinoma cell line (FU-UR-1) with the reciprocal ASPL-TFE3 fusion transcript. Oncol Rep. 2004;11:1169–75.

33. Hirobe M, Masumori N, Tanaka T, Kitamura H, Tsukamoto T. Establishment of an ASPL-TFE3 renal cell carcinoma cell line (S-TFE). Cancer Biol Ther. 2013;14:502–10.

34. Calandrini C, Schutgens F, Oka R, Margaritis T, Candelli T, Mathijsen L, et al. An organoid biobank for childhood kidney cancers that captures disease and tissue heterogeneity. Nat Commun. 2020;11:1310.

35. Fujiwara T, Kunisada T, Nakata E, Nishida K, Yanai H, Nakamura T, et al. Advances in treatment of alveolar soft part sarcoma: an updated review. Jpn J Clin Oncol. 2023;53:1009–18.

36. Argani P, Gross JM, Baraban E, Rooper LM, Chen S, Lin M-T, et al. TFE3 -Rearranged PEComa/PEComa-like Neoplasms : Report of 25 New Cases Expanding the Clinicopathologic Spectrum and Highlighting its Association With Prior Exposure to Chemotherapy. Am J Surg Pathol. 2024;48:777–89.

37. Neil E, Kouskoff V. Current Model Systems for Investigating Epithelioid Haemangioendothelioma. Cancers (Basel). 2023;15:3005.

38. Panagopoulos I, Gorunova L, Lund-Iversen M, Bassarova A, Heim S. Fusion of the Genes PHF1 and TFE3 in Malignant Chondroid Syringoma. Cancer Genomics Proteomics. 2019;16:345–51.

39. Suurmeijer AJH, Song W, Sung Y-S, Zhang L, Swanson D, Fletcher CDM, et al. Novel recurrent PHF1-TFE3 fusions in ossifying fibromyxoid tumors. Genes Chromosomes Cancer. 2019;58:643–9.

40. Doench JG, Fusi N, Sullender M, Hegde M, Vaimberg EW, Donovan KF, et al. Optimized sgRNA design to maximize activity and minimize off-target effects of CRISPR-Cas9. Nat Biotechnol. 2016;34:184–91.

41. DepMap, Broad (2024). Current DepMap Release data, including CRISPR Screens, PRISM Drug Screens, Copy Number, Mutation, Expression, and Fusions. DepMap 23Q2 Public. Figshare+. Dataset.;

42. Hart T, Chandrashekhar M, Aregger M, Steinhart Z, Brown KR, MacLeod G, et al. High-Resolution CRISPR Screens Reveal Fitness Genes and Genotype-Specific Cancer Liabilities. Cell. 2015;163:1515–26.

43. Dempster JM, Pacini C, Pantel S, Behan FM, Green T, Krill-Burger J, et al. Agreement between two large pan-cancer CRISPR-Cas9 gene dependency data sets. Nat Commun. 2019;10:5817.

44. Achom M, Sadagopan A, Bao C, McBride F, Xu Q, Konda P, et al. A genetic basis for cancer sex differences revealed in Xp11 translocation renal cell carcinoma [Internet]. bioRxiv; 2023 [cited 2023 Aug 9]. page 2023.08.04.552029. Available from: https://www.biorxiv.org/content/10.1101/2023.08.04.552029v1

45. Kuleshov MV, Jones MR, Rouillard AD, Fernandez NF, Duan Q, Wang Z, et al. Enrichr: a comprehensive gene set enrichment analysis web server 2016 update. Nucleic Acids Res. 2016;44:W90-97.

46. Read AD, Bentley RE, Archer SL, Dunham-Snary KJ. Mitochondrial iron-sulfur clusters: Structure, function, and an emerging role in vascular biology. Redox Biol. 2021;47:102164.

47. Li J, Huang K, McBride F, Sadagopan A, Gallant DS, Thakur M, et al. TFE3 fusions direct an oncogenic transcriptional program that drives OXPHOS and unveils vulnerabilities in translocation renal cell carcinoma [Internet]. bioRxiv; 2024 [cited 2024 Aug 10]. page 2024.08.09.607311. Available from: https://www.biorxiv.org/content/10.1101/2024.08.09.607311v1

48. Tong G-X, Yu WM, Beaubier NT, Weeden EM, Hamele-Bena D, Mansukhani MM, et al. Expression of PAX8 in normal and neoplastic renal tissues: an immunohistochemical study. Modern Pathology. 2009;22:1218–27.

49. Clissold RL, Hamilton AJ, Hattersley AT, Ellard S, Bingham C. HNF1B-associated renal and extra-renal disease—an expanding clinical spectrum. Nat Rev Nephrol. 2015;11:102–12.

50. Patel SA, Hirosue S, Rodrigues P, Vojtasova E, Richardson EK, Ge J, et al. The renal lineage factor PAX8 controls oncogenic signalling in kidney cancer. Nature. 2022;606:999–1006.

51. Prakasam G, Mishra A, Christie A, Miyata J, Carrillo D, Tcheuyap VT, et al. Comparative genomics incorporating translocation renal cell carcinoma mouse model reveals molecular mechanisms of tumorigenesis. J Clin Invest. 2024;134:e170559.

52. Riscal R, Bull CJ, Mesaros C, Finan JM, Carens M, Ho ES, et al. Cholesterol Auxotrophy as a Targetable Vulnerability in Clear Cell Renal Cell Carcinoma. Cancer Discovery. 2021;11:3106–25.

53. Thompson JM, Alvarez A, Singha MK, Pavesic MW, Nguyen QH, Nelson LJ, et al. Targeting the Mevalonate Pathway Suppresses VHL-Deficient CC-RCC through an HIF-Dependent Mechanism. Molecular Cancer Therapeutics. 2018;17:1781–92.

54. Dempster JM, Krill-Burger JM, McFarland JM, Warren A, Boehm JS, Vazquez F, et al. Gene expression has more power for predicting *in vitro* cancer cell vulnerabilities than genomics [Internet]. 2020 [cited 2024 Jun 26]. Available from: http://biorxiv.org/lookup/doi/10.1101/2020.02.21.959627

55. Warren A, Chen Y, Jones A, Shibue T, Hahn WC, Boehm JS, et al. Global computational alignment of tumor and cell line transcriptional profiles. Nat Commun. 2021;12:22.

56. Shi X, Gekas C, Verduzco D, Petiwala S, Jeffries C, Lu C, et al. Building a translational cancer dependency map for The Cancer Genome Atlas. Nat Cancer. Nature Publishing Group; 2024;1–19.

57. Wang W, Albadari N, Du Y, Fowler JF, Sang HT, Xian W, et al. MDM2 Inhibitors for Cancer Therapy: The Past, Present, and Future. Gottesman M, editor. Pharmacol Rev. 2024;76:414–53.

58. Romero R, Sánchez-Rivera FJ, Westcott PMK, Mercer KL, Bhutkar A, Muir A, et al. Keap1 mutation renders lung adenocarcinomas dependent on Slc33a1. Nat Cancer. 2020;1:589–602.

59. Ricketts CJ, De Cubas AA, Fan H, Smith CC, Lang M, Reznik E, et al. The Cancer Genome Atlas Comprehensive Molecular Characterization of Renal Cell Carcinoma. Cell Rep. 2018;23:313-326.e5.

60. Gounder MM, Bauer TM, Schwartz GK, Weise AM, LoRusso P, Kumar P, et al. A First-in-Human Phase I Study of Milademetan, an MDM2 Inhibitor, in Patients With Advanced Liposarcoma, Solid Tumors, or Lymphomas. JCO. 2023;41:1714–24.

61. Drexler H, Fombonne S, Matsuo Y, Hu Z-B, Hamaguchi H, Uphoff C. p53 alterations in human leukemia–lymphoma cell lines: in vitroartifact or prerequisite for cell immortalization? Leukemia. 2000;14:198–206.

62. Achom M, Sadagopan A, Bao C, McBride F, Li J, Konda P, et al. A genetic basis for sex differences in Xp11 translocation renal cell carcinoma. Cell [Internet]. Elsevier; 2024 [cited 2024 Aug 20];0. Available from: https://www.cell.com/cell/abstract/S0092-8674(24)00832-8

63. Maitituoheti M, Keung EZ, Tang M, Yan L, Alam H, Han G, et al. Enhancer Reprogramming Confers Dependence on Glycolysis and IGF Signaling in KMT2D Mutant Melanoma. Cell Rep. 2020;33:108293.

64. Schoolmeester JK, Dao LN, Sukov WR, Wang L, Park KJ, Murali R, et al. TFE3 translocation-associated perivascular epithelioid cell neoplasm (PEComa) of the gynecologic tract: morphology, immunophenotype, differential diagnosis. Am J Surg Pathol. 2015;39:394–404.

65. Antonescu CR, Le Loarer F, Mosquera J-M, Sboner A, Zhang L, Chen C-L, et al. Novel YAP1-TFE3 fusion defines a distinct subset of epithelioid hemangioendothelioma. Genes Chromosomes Cancer. 2013;52:775–84.

66. Tanaka M, Chuaychob S, Homme M, Yamazaki Y, Lyu R, Yamashita K, et al. ASPSCR1::TFE3 orchestrates the angiogenic program of alveolar soft part sarcoma. Nat Commun. 2023;14:1957.

67. Wang X, Fang R, Zhang R, Ye S, Li R, Wang X, et al. Malignant melanotic Xp11 neoplasms exhibit a clinicopathologic spectrum and gene expression profiling akin to alveolar soft part sarcoma: a proposal for reclassification. J Pathol. 2020;251:365–77.

68. Lee SJ, Yang WI, Chung W-S, Kim SK. Epithelioid hemangioendotheliomas with TFE3 gene translocations are compossible with CAMTA1 gene rearrangements. Oncotarget. 2016;7:7480–8.

69. Viswanathan VS, Ryan MJ, Dhruv HD, Gill S, Eichhoff OM, Seashore-Ludlow B, et al. Dependency of a therapy-resistant state of cancer cells on a lipid peroxidase pathway. Nature. 2017;547:453–7.

70. Caenepeel S, Karen R, Belmontes B, Verlinsky A, Tan H, Yang Y, et al. Abstract 6218: Discovery and preclinical evaluation of AMG 397, a potent, selective and orally bioavailable MCL1 inhibitor. Cancer Research. 2020;80:6218–6218.

71. Grubb T, Maganti S, Krill-Burger JM, Fraser C, Stransky L, Radivoyevitch T, et al. A Mesenchymal Tumor Cell State Confers Increased Dependency on the BCL-XL Antiapoptotic Protein in Kidney Cancer. Clin Cancer Res. 2022;28:4689–701.

72. Shakhova O, Zingg D, Schaefer SM, Hari L, Civenni G, Blunschi J, et al. Sox10 promotes the formation and maintenance of giant congenital naevi and melanoma. Nat Cell Biol. 2012;14:882–90.

73. Cronin JC, Watkins-Chow DE, Incao A, Hasskamp JH, Schönewolf N, Aoude LG, et al. SOX10 ablation arrests cell cycle, induces senescence, and suppresses melanomagenesis. Cancer Res. 2013;73:5709–18.

74. Morin PJ, Sparks AB, Korinek V, Barker N, Clevers H, Vogelstein B, et al. Activation of beta-catenin-Tcf signaling in colon cancer by mutations in beta-catenin or APC. Science. 1997;275:1787–90.

75. Korinek V, Barker N, Morin PJ, van Wichen D, de Weger R, Kinzler KW, et al. Constitutive transcriptional activation by a beta-catenin-Tcf complex in APC-/- colon carcinoma. Science. 1997;275:1784–7.

76. Cancer Genome Atlas Network. Comprehensive molecular characterization of human colon and rectal cancer. Nature. 2012;487:330–7.

77. Huang T, Hou Y, Wang X, Wang L, Yi C, Wang C, et al. Direct Interaction of Sox10 With Cadherin-19 Mediates Early Sacral Neural Crest Cell Migration: Implications for Enteric Nervous System Development Defects. Gastroenterology. 2022;162:179-192.e11.

78. Stamos JL, Weis WI. The β-catenin destruction complex. Cold Spring Harb Perspect Biol. 2013;5:a007898.

79. Kim J-S, Crooks H, Dracheva T, Nishanian TG, Singh B, Jen J, et al. Oncogenic beta-catenin is required for bone morphogenetic protein 4 expression in human cancer cells. Cancer Res. 2002;62:2744–8.

80. Van Raay TJ, Fortino NJ, Miller BW, Ma H, Lau G, Li C, et al. Naked1 Antagonizes Wnt Signaling by Preventing Nuclear Accumulation of β-Catenin. Koch K-W, editor. PLoS ONE. 2011;6:e18650.

81. Morrison L, Loibl S, Turner NC. The CDK4/6 inhibitor revolution — a game-changing era for breast cancer treatment. Nat Rev Clin Oncol. 2024;21:89–105.

82. Ghandi M, Huang FW, Jané-Valbuena J, Kryukov GV, Lo CC, McDonald ER, et al. Next-generation characterization of the Cancer Cell Line Encyclopedia. Nature. 2019;569:503–8.

83. Blache P, van de Wetering M, Duluc I, Domon C, Berta P, Freund J-N, et al. SOX9 is an intestine crypt transcription factor, is regulated by the Wnt pathway, and represses the CDX2 and MUC2 genes. J Cell Biol. 2004;166:37–47.

84. Kurnit KC, Sinno AK, Fellman BM, Varghese A, Stone R, Sood AK, et al. Effects of Gastrointestinal-Type Chemotherapy in Women With Ovarian Mucinous Carcinoma. Obstet Gynecol. 2019;134:1253–9.

85. Kurmasheva RT, Sammons M, Favours E, Wu J, Kurmashev D, Cosmopoulos K, et al. Initial testing (stage 1) of tazemetostat (EPZ-6438), a novel EZH2 inhibitor, by the Pediatric Preclinical Testing Program. Pediatr Blood Cancer. 2017;64.

86. Schmidt A, Behrendt L, Eybe J, Warmann SW, Schleicher S, Fuchs J, et al. The Effect of Direct and Indirect EZH2 Inhibition in Rhabdomyosarcoma Cell Lines. Cancers (Basel). 2021;14:41.

87. Torchia J, Golbourn B, Feng S, Ho KC, Sin-Chan P, Vasiljevic A, et al. Integrated (epi)-Genomic Analyses Identify Subgroup-Specific Therapeutic Targets in CNS Rhabdoid Tumors. Cancer Cell. 2016;30:891–908.

88. Knutson SK, Warholic NM, Wigle TJ, Klaus CR, Allain CJ, Raimondi A, et al. Durable tumor regression in genetically altered malignant rhabdoid tumors by inhibition of methyltransferase EZH2. Proc Natl Acad Sci USA. 2013;110:7922–7.

89. Jones BA, Varambally S, Arend RC. Histone Methyltransferase EZH2: A Therapeutic Target for Ovarian Cancer. Mol Cancer Ther. 2018;17:591–602.

90. Sasaki M, Kato D, Murakami K, Yoshida H, Takase S, Otsubo T, et al. Targeting dependency on a paralog pair of CBP/p300 against de-repression of KREMEN2 in SMARCB1-deficient cancers. Nat Commun. 2024;15:4770.

91. Voss MH, Chen D, Marker M, Hakimi AA, Lee C-H, Hsieh JJ, et al. Circulating biomarkers and outcome from a randomised phase II trial of sunitinib vs everolimus for patients with metastatic renal cell carcinoma. Br J Cancer. 2016;114:642–9.

92. Motzer RJ, Escudier B, McDermott DF, George S, Hammers HJ, Srinivas S, et al. Nivolumab versus Everolimus in Advanced Renal-Cell Carcinoma. N Engl J Med. 2015;373:1803–13.

93. Sinha R, Winer AG, Chevinsky M, Jakubowski C, Chen Y-B, Dong Y, et al. Analysis of renal cancer cell lines from two major resources enables genomics-guided cell line selection. Nat Commun. Nature Publishing Group; 2017;8:15165.

94. Bakouny Z, Braun DA, Shukla SA, Pan W, Gao X, Hou Y, et al. Integrative molecular characterization of sarcomatoid and rhabdoid renal cell carcinoma. Nature Communications. Nature Publishing Group; 2021;12:808.

95. Maughan BL, Sirohi D. Papillary Renal Cell Carcinoma: A Review of Prospective Clinical Trials. Curr Treat Options in Oncol. 2023;24:1199–212.

96. Henske EP, Cheng L, Hakimi AA, Choueiri TK, Braun DA. Chromophobe renal cell carcinoma. Cancer Cell. 2023;41:1383–8.

97. Bártů M, Hojný J, Hájková N, Michálková R, Krkavcová E, Hadravský L, et al. Analysis of expression, epigenetic, and genetic changes of HNF1B in 130 kidney tumours. Sci Rep. 2020;10:17151.

98. Wang C-C, Mao T-L, Yang W-C, Jeng Y-M. Underexpression of hepatocyte nuclear factor-1β in chromophobe renal cell carcinoma. Histopathology. 2013;62:589–94.

99. Kalev P, Hyer ML, Gross S, Konteatis Z, Chen C-C, Fletcher M, et al. MAT2A Inhibition Blocks the Growth of MTAP-Deleted Cancer Cells by Reducing PRMT5-Dependent mRNA Splicing and Inducing DNA Damage. Cancer Cell. 2021;39:209-224.e11.

100. Adam J, Hatipoglu E, O'Flaherty L, Ternette N, Sahgal N, Lockstone H, et al. Renal cyst formation in Fh1-deficient mice is independent of the Hif/Phd pathway: roles for fumarate in KEAP1 succination and Nrf2 signaling. Cancer Cell. 2011;20:524–37.

101. Chen F, Zhang Y, Şenbabaoğlu Y, Ciriello G, Yang L, Reznik E, et al. Multilevel Genomics-Based Taxonomy of Renal Cell Carcinoma. Cell Reports. 2016;14:2476–89.

102. Fabrizio FP, Costantini M, Copetti M, la Torre A, Sparaneo A, Fontana A, et al. Keap1/Nrf2 pathway in kidney cancer: frequent methylation of KEAP1 gene promoter in clear renal cell carcinoma. Oncotarget. 2017;8:11187–98.

103. Pillai R, Hayashi M, Zavitsanou A-M, Papagiannakopoulos T. NRF2: KEAPing Tumors Protected. Cancer Discovery. 2022;12:625–43.

104. M G, T P, L B-P. Reductive stress in cancer: coming out of the shadows. Trends in cancer [Internet]. Trends Cancer; 2024 [cited 2024 Feb 28];10. Available from: https://pubmed.ncbi.nlm.nih.gov/37925319/

105. Weiss-Sadan T, Ge M, Hayashi M, Gohar M, Yao C-H, de Groot A, et al. NRF2 activation induces NADH-reductive stress, providing a metabolic vulnerability in lung cancer. Cell Metabolism. 2023;S1550413123000128.

106. Köferle A, Schlattl A, Hörmann A, Thatikonda V, Popa A, Spreitzer F, et al. Interrogation of cancer gene dependencies reveals paralog interactions of autosome and sex chromosome-encoded genes. Cell Rep. 2022;39:110636.

107. Qi M, Pang J, Mitsiades I, Lane AA, Rheinbay E. Loss of chromosome Y in primary tumors. Cell. 2023;S0092-8674(23)00646-3.

108. Donehower LA, Soussi T, Korkut A, Liu Y, Schultz A, Cardenas M, et al. Integrated Analysis of TP53 Gene and Pathway Alterations in The Cancer Genome Atlas. Cell Rep. 2019;28:1370-1384.e5.

109. Zou Y, Palte MJ, Deik AA, Li H, Eaton JK, Wang W, et al. A GPX4-dependent cancer cell state underlies the clear-cell morphology and confers sensitivity to ferroptosis. Nat Commun. Nature Publishing Group; 2019;10:1617.

110. Mavrakis KJ, McDonald ER, Schlabach MR, Billy E, Hoffman GR, deWeck A, et al. Disordered methionine metabolism in MTAP/CDKN2A-deleted cancers leads to dependence on PRMT5. Science. American Association for the Advancement of Science; 2016;351:1208–13.

111. Kryukov GV, Wilson FH, Ruth JR, Paulk J, Tsherniak A, Marlow SE, et al. MTAP deletion confers enhanced dependency on the PRMT5 arginine methyltransferase in cancer cells. Science. American Association for the Advancement of Science; 2016;351:1214–8.

112. Ronk H, Rosenblum JS, Kung T, Zhuang Z. Targeting PP2A for cancer therapeutic modulation. Cancer Biol Med. 2022;19:1428–39.

113. Ho WS, Wang H, Maggio D, Kovach JS, Zhang Q, Song Q, et al. Pharmacologic inhibition of protein phosphatase-2A achieves durable immune-mediated antitumor activity when combined with PD-1 blockade. Nat Commun. 2018;9:2126.

114. Steingrímsson E, Tessarollo L, Pathak B, Hou L, Arnheiter H, Copeland NG, et al. Mitf and Tfe3, two members of the Mitf-Tfe family of bHLH-Zip transcription factors, have important but functionally redundant roles in osteoclast development. PNAS. National Academy of Sciences; 2002;99:4477–82.

115. Pastore N, Vainshtein A, Klisch TJ, Armani A, Huynh T, Herz NJ, et al. TFE3 regulates whole-body energy metabolism in cooperation with TFEB. EMBO Mol Med. 2017;9:605–21.

116. Settembre C, De Cegli R, Mansueto G, Saha PK, Vetrini F, Visvikis O, et al. TFEB controls cellular lipid metabolism through a starvation-induced autoregulatory loop. Nat Cell Biol. 2013;15:647–58.

117. Raben N, Puertollano R. TFEB and TFE3: Linking Lysosomes to Cellular Adaptation to Stress. Annu Rev Cell Dev Biol. 2016;32:255–78.

118. Chiu Y-C, Zheng S, Wang L-J, Iskra BS, Rao MK, Houghton PJ, et al. Predicting and characterizing a cancer dependency map of tumors with deep learning. Sci Adv. 2021;7:eabh1275.

119. Yuda J, Will C, Phillips DC, Abraham L, Alvey C, Avigdor A, et al. Selective MCL-1 inhibitor ABBV-467 is efficacious in tumor models but is associated with cardiac troponin increases in patients. Commun Med. 2023;3:154.

120. Rauh U, Wei G, Serrano-Wu M, Kosmidis G, Kaulfuss S, Siegel F, et al. BRD-810 is a highly selective MCL1 inhibitor with optimized in vivo clearance and robust efficacy in solid and hematological tumor models. Nat Cancer [Internet]. 2024 [cited 2024 Sep 5]; Available from: https://www.nature.com/articles/s43018-024-00814-0

121. Msaouel P, Genovese G, Tannir NM. Renal Cell Carcinoma of Variant Histology: Biology and Therapies. Hematol Oncol Clin North Am. 2023;S0889-8588(23)00053-9.

122. Msaouel P, Malouf GG, Su X, Yao H, Tripathi DN, Soeung M, et al. Comprehensive Molecular Characterization Identifies Distinct Genomic and Immune Hallmarks of Renal Medullary Carcinoma. Cancer Cell. 2020;37:720-734.e13.

123. Coutinho DF, Mundi PS, Marks LJ, Burke C, Ortiz MV, Diolaiti D, et al. Validation of a non-oncogene encoded vulnerability to exportin 1 inhibition in pediatric renal tumors. Med. 2022;3:774-791.e7.

124. Wang J, Papanicolau-Sengos A, Chintala S, Wei L, Liu B, Hu Q, et al. Collecting duct carcinoma of the kidney is associated with CDKN2A deletion and SLC family gene up-regulation. Oncotarget. 2016;7:29901–15.

125. Doench JG, Hartenian E, Graham DB, Tothova Z, Hegde M, Smith I, et al. Rational design of highly active sgRNAs for CRISPR-Cas9–mediated gene inactivation. Nat Biotechnol. 2014;32:1262–7.

126. Doench JG, Fusi N, Sullender M, Hegde M, Vaimberg EW, Donovan KF, et al. Optimized sgRNA design to maximize activity and minimize off-target effects of CRISPR-Cas9. Nat Biotechnol. 2016;34:184–91.

127. Sanson KR, Hanna RE, Hegde M, Donovan KF, Strand C, Sullender ME, et al. Optimized libraries for CRISPR-Cas9 genetic screens with multiple modalities. Nat Commun. 2018;9:5416.

128. Shalem O, Sanjana NE, Hartenian E, Shi X, Scott DA, Mikkelsen TS, et al. Genome-Scale CRISPR-Cas9 Knockout Screening in Human Cells. Science. 2014;343:84–7.

129. Sanjana NE, Shalem O, Zhang F. Improved vectors and genome-wide libraries for CRISPR screening. Nat Methods. 2014;11:783–4.

130. Li W, Xu H, Xiao T, Cong L, Love MI, Zhang F, et al. MAGeCK enables robust identification of essential genes from genome-scale CRISPR/Cas9 knockout screens. Genome Biol. 2014;15:554.

131. Li H, Durbin R. Fast and accurate short read alignment with Burrows-Wheeler transform. Bioinformatics. 2009;25:1754–60.

132. Riester M, Singh AP, Brannon AR, Yu K, Campbell CD, Chiang DY, et al. PureCN: copy number calling and SNV classification using targeted short read sequencing. Source Code Biol Med. 2016;11:13.

133. Li B, Dewey CN. RSEM: accurate transcript quantification from RNA-Seq data with or without a reference genome. BMC Bioinformatics. 2011;12:323.

134. Dobin A, Davis CA, Schlesinger F, Drenkow J, Zaleski C, Jha S, et al. STAR: ultrafast universal RNA-seq aligner. Bioinformatics. 2013;29:15–21.

135. Tatlow PJ, Piccolo SR. A cloud-based workflow to quantify transcript-expression levels in public cancer compendia. Sci Rep. 2016;6:39259.

136. Zhang Y, Parmigiani G, Johnson WE. ComBat-seq: batch effect adjustment for RNA-seq count data. NAR Genom Bioinform. 2020;2:lqaa078.

137. Braun DA, Hou Y, Bakouny Z, Ficial M, Sant' Angelo M, Forman J, et al. Interplay of somatic alterations and immune infiltration modulates response to PD-1 blockade in advanced clear cell renal cell carcinoma. Nat Med. Nature Publishing Group; 2020;26:909–18.

138. Davidson-Pilon C. lifelines: survival analysis in Python. Journal of Open Source Software. 2019;4:1317.

139. Seavey CN, Pobbati AV, Hallett A, Ma S, Reynolds JP, Kanai R, et al. WWTR1(TAZ)-CAMTA1 gene fusion is sufficient to dysregulate YAP/TAZ signaling and drive epithelioid hemangioendothelioma tumorigenesis. Genes Dev. 2021;35:512–27.

140. Braun DA, Ishii Y, Walsh AM, Van Allen EM, Wu CJ, Shukla SA, et al. Clinical Validation of *PBRM1* Alterations as a Marker of Immune Checkpoint Inhibitor Response in Renal Cell Carcinoma. JAMA Oncol. 2019;5:1631.

141. Motzer RJ, Tannir NM, McDermott DF, Arén Frontera O, Melichar B, Choueiri TK, et al. Nivolumab plus Ipilimumab versus Sunitinib in Advanced Renal-Cell Carcinoma. N Engl J Med. 2018;378:1277–90.

142. Cancer Genome Atlas Research Network, Weinstein JN, Collisson EA, Mills GB, Shaw KRM, Ozenberger BA, et al. The Cancer Genome Atlas Pan-Cancer analysis project. Nat Genet. 2013;45:1113–20.

143. Cancer Genome Atlas Research Network, Linehan WM, Spellman PT, Ricketts CJ, Creighton CJ, Fei SS, et al. Comprehensive Molecular Characterization of Papillary Renal-Cell Carcinoma. N Engl J Med. 2016;374:135–45.

144. Davis CF, Ricketts CJ, Wang M, Yang L, Cherniack AD, Shen H, et al. The somatic genomic landscape of chromophobe renal cell carcinoma. Cancer Cell. 2014;26:319–30.

145. Liu YJ, Ussakli C, Antic T, Liu Y, Wu Y, True L, et al. Sporadic oncocytic tumors with features intermediate between oncocytoma and chromophobe renal cell carcinoma: comprehensive clinicopathological and genomic profiling. Hum Pathol. 2020;104:18–29.

Acknowledgements:

Schematic illustrations were created with BioRender.com.

Funding: S.R.V: Doris Duke Charitable Foundation (Clinician-Scientist Development Award grant number: 2020101), Department of Defense Kidney Cancer Research Program (DoD KCRP) (W81XWH-19-1-0815 / KC180130; W81XWH-22-1-1016 / KC210039), NCI (R01CA286652; R01CA279044; R01CA269505), DF/HCC Kidney SPORE (2P50CA101942-16), Rally Foundation Independent Investigator Grant (23IN3). J.L.: Department of Defense Kidney Cancer Research Program (DoD KCRP) (W81XWH-22-1-0399). P.K. Department of Defense Kidney Cancer Research Program (DoD KCRP) Postdoctoral and Clinical Fellowship (HT94252310066). C.N.W.: American Association for Cancer Research (AACR) Exelixis Renal Cell Carcinoma Research Fellowship (1306525). T.K.C.: Dana-Farber/Harvard Cancer Center Kidney SPORE (2P50CA101942-16) and Program 5P30CA00651656, the Kohlberg Chair at Harvard Medical School and the Trust Family, Michael Brigham, Pan Mass Challenge, Hinda and Arthur Marcus Fund, and Loker Pinard Funds for Kidney Cancer Research at DFCI.

Author contributions: S.R.V designed and supervised the study. B.L., A.S., S.R.V wrote the manuscript with input from all co-authors. A.S. performed analysis of genome-scale CRISPR screening data, dependency prediction and developed the predictive model used in this study. Y.C. and P.K. assisted in analysis of dependency data. B.L. led experimental work including genome-scale CRISPR screening and dependency validation. J.L., C.N.W., Y.W. assisted in experimental work and contributed to experimental design. T.K.C., A.S., provided clinical trial data and/or analysis. J.G.D. contributed to design of screening and validation studies.

Data Availability: Chronos scores from tRCC CRISPR screen are available in **Supplementary Table S1.** External datasets analyzed are public and are available from the respective cited publications. Chronos score predictions for all external datasets are available in **Supplementary Table S4.**

Code Availability: Code for the developed tool will be publicly available in Github at time of publication: https://github.com/SViswanathanLab/TrPLet.

Declaration of Interests: Aspects of this work are the subject of a pending patent application (A.S., S.R.V.). S.R.V.: has consulted for Jnana Therapeutics within the past 3 years; receives research support from Bayer. T.K.C. reports institutional and personal paid or unpaid support for research, advisory board participation, consultancy, and honoraria within the past 5 years from Alkermes, Arcus Bio, AstraZeneca, Aravive, Aveo, Bayer, Bristol Myers Squibb, Calithera, Circle Pharma, Deciphera Pharmaceuticals, Eisai, EMD Serono, Exelixis, GlaxoSmithKline, Gilead, HiberCell, IQVIA, Infinity, Ipsen, Jansen, Kanaph, Lilly, Merck, Nikang, Neomorph, Nuscan and Precede Bio, Novartis, Oncohost, Pfizer, Roche, Sanofi Aventis, Scholar Rock, Surface Oncology, Takeda, and Tempest and equity in Tempest, Pionyr, Osel, Precede Bio, CureResponse, InnDura Therapeutics, and Primium.

List of Supplementary Materials

Materials and Methods

907 Supplementary Fig. S1 to Fig. S6
908 Supplementary Table S1 to Table S4
909 References 125-145
910

Main Figures and Captions

Fig.1 | Genome-scale genetic screening reveals selective essentialities of tRCC cells

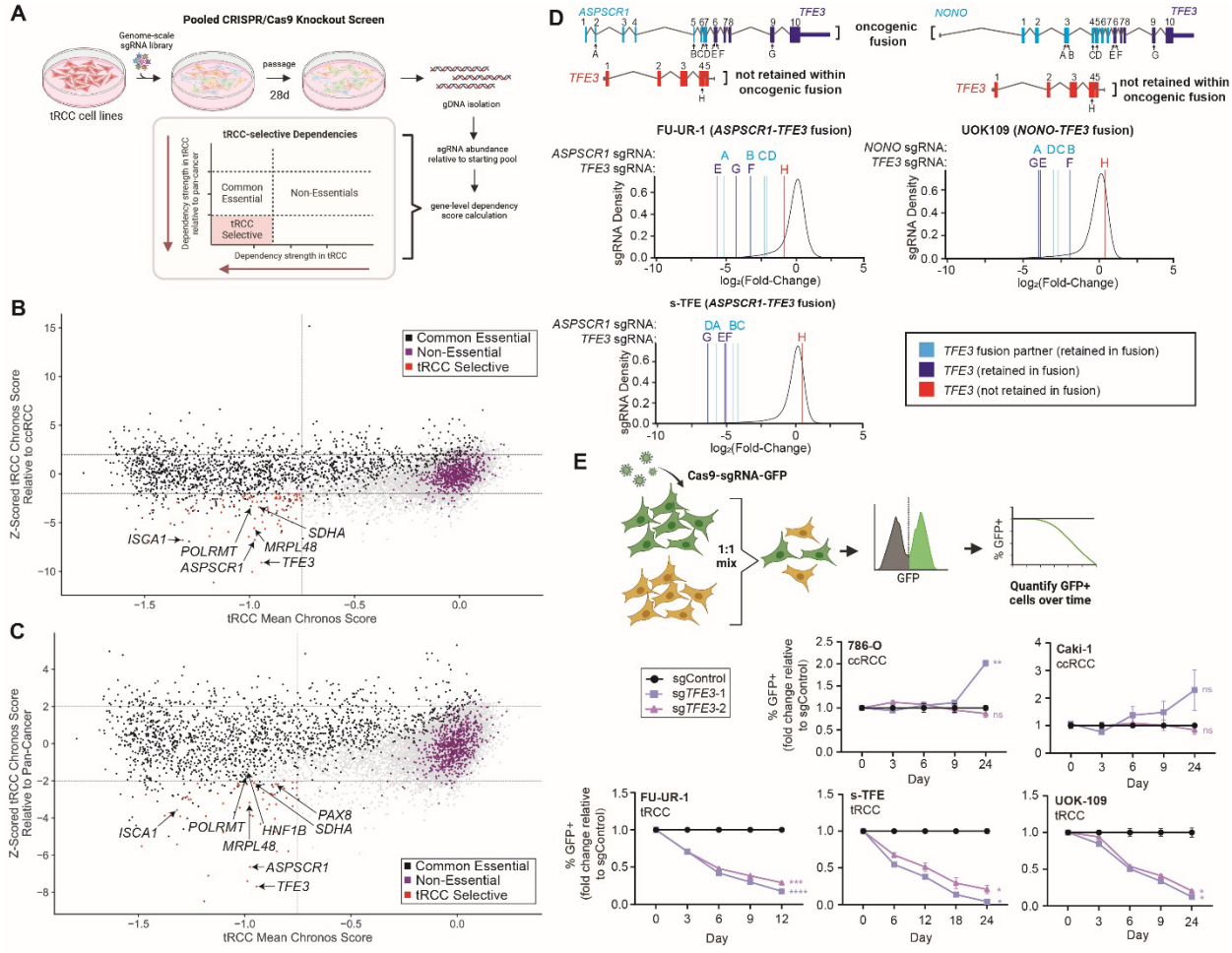

(A) Workflow for CRISPR screens and analysis to identify tRCC-selective genetic dependencies.

(B-C) Landscape of tRCC-selective dependencies. Mean Chronos score for each gene across the 3 tRCC cell lines screened in this study is plotted against the Z-scored Chronos score for that gene (Z-score calculated relative to DepMap ccRCC cell lines in **B** and relative to all DepMap cell lines in **C**). Non-essential-genes are colored in purple while common essential genes are colored in black (42). tRCC-selective dependencies (defined as Z-score < -2; absolute Chronos score < -0.75) are colored in red.

(D) Log-fold change for individual sgRNAs targeting either *TFE3* (E, F, G, H) or fusion partner (A, B, C, D) in tRCC CRISPR screens. The exons targeted by each sgRNA are indicated in the schematics. For each cell line, the top schematic represents the exons coding for the oncogenic fusion while the bottom schematic represents the N-terminal exons of *TFE3* not included in the oncogenic fusion. Density plot shows the distribution for LFC of all sgRNAs assessed in the CRISPR screen in each cell line while vertical lines represent log-fold change for individual sgRNAs. Note: Figure shows the *ASPSCR1-TFE3* fusion in s-TFE cells; the *ASPSCR1-TFE3* fusion in FU-UR-1 cells retains exon 5 of *TFE3* exon 5.

(E) Competitive growth assay to assess the effects of *TFE3* knockout in two ccRCC lines (786-O, Caki-1) and three tRCC lines (UOK109, FU-UR-1, s-TFE). Cells expressing Cas9/sgRNA and GFP were mixed in a 1:1 ratio

930 with parental cells and proportion relative to sgControl cells was calculated at each time point via flow
931 cytometry. Shown as mean +/- s.d., n=2 biological replicates per condition. *P*-values were calculated by
932 Welch's (two-tailed unpaired) t-test as compared with sgControl samples at the final time point. *$P < 0.05$, **$P < 0.01$, ***$P < 0.001$, ****$P < 0.0001$.

934

Fig.2 | Validation of selective tRCC dependencies

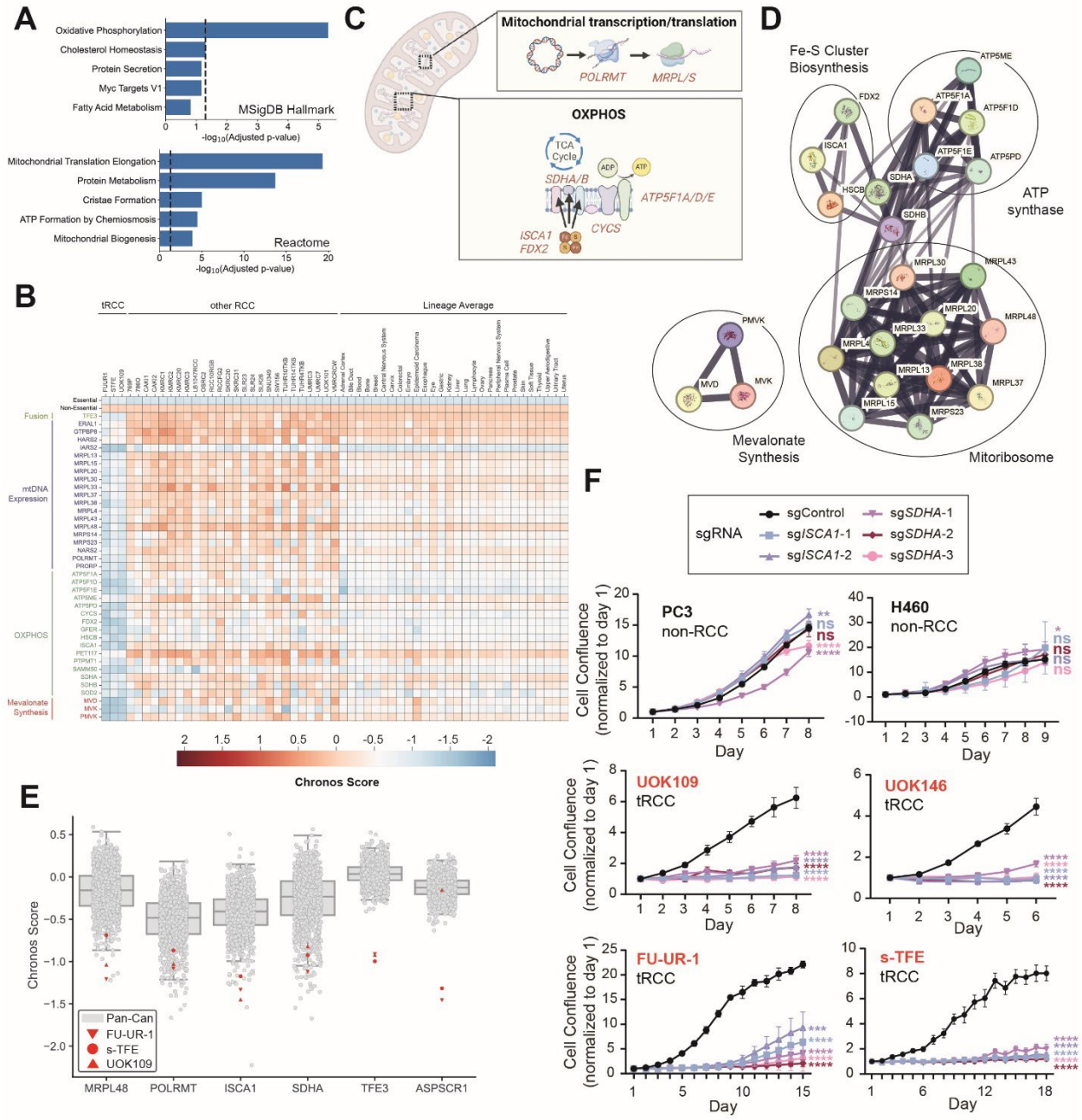

(A) Pathway enrichment (Enrichr) on gene dependencies shared across all three tRCC cell lines (defined as genes with ΔChronos ≤ -0.5 between every tRCC cell line and DepMap ccRCC mean).

(B) Heat map of tRCC-selective dependencies (defined as genes with ΔChronos ≤ -0.5 between every tRCC cell line and DepMap ccRCC mean), for selected pathways (remaining genes/pathways shown in **Supplementary Fig. S1B**). Chronos scores for individual tRCC cell lines, DepMap RCC cell lines, and average Chronos score for each of 28 lineages screened in DepMap are shown. The top two rows indicate mean Chronos scores for essential and non-essential genes in each column, shown for reference.

(C) Schematic depicting tRCC-selective dependencies that fall within pathways related to mitochondrial metabolism.

(D) Protein-protein interaction network amongst interacting tRCC-selective gene dependencies (genes with ΔChronos ≤ -0.5 between every tRCC cell line and DepMap ccRCC mean) involved in mtDNA expression, OXPHOS, and mevalonate synthesis (STRINGdb).

(E) Distribution of Chronos scores for indicated genes (*POLRMT, MRPL48, ISCA1, SDHA, TFE3, ASPSCR1*) across all DepMap cell lines (gray) and tRCC cell lines screened in this study (red).

(F) Relative confluence of non-RCC cells (PC3, H460), and tRCC cells (UOK109, UOK146, FU-UR-1, s-TFE) after infection with lentivirus expressing Cas9 and either non-targeting control sgRNA, *ISCA1* sgRNAs, or *SDHA* sgRNAs. Confluence was normalized to day 1, shown as mean +/- s.d., n=6 biological replicates per condition. *P*-values were calculated by Welch's (two-tailed unpaired) t test as compared with sgControl samples for the last assay day. **P* < 0.05, ***P* < 0.01, ****P* < 0.001, *****P* < 0.0001.

Fig.3 | A machine-learning model uncovers additional strong dependencies in tRCC subsets

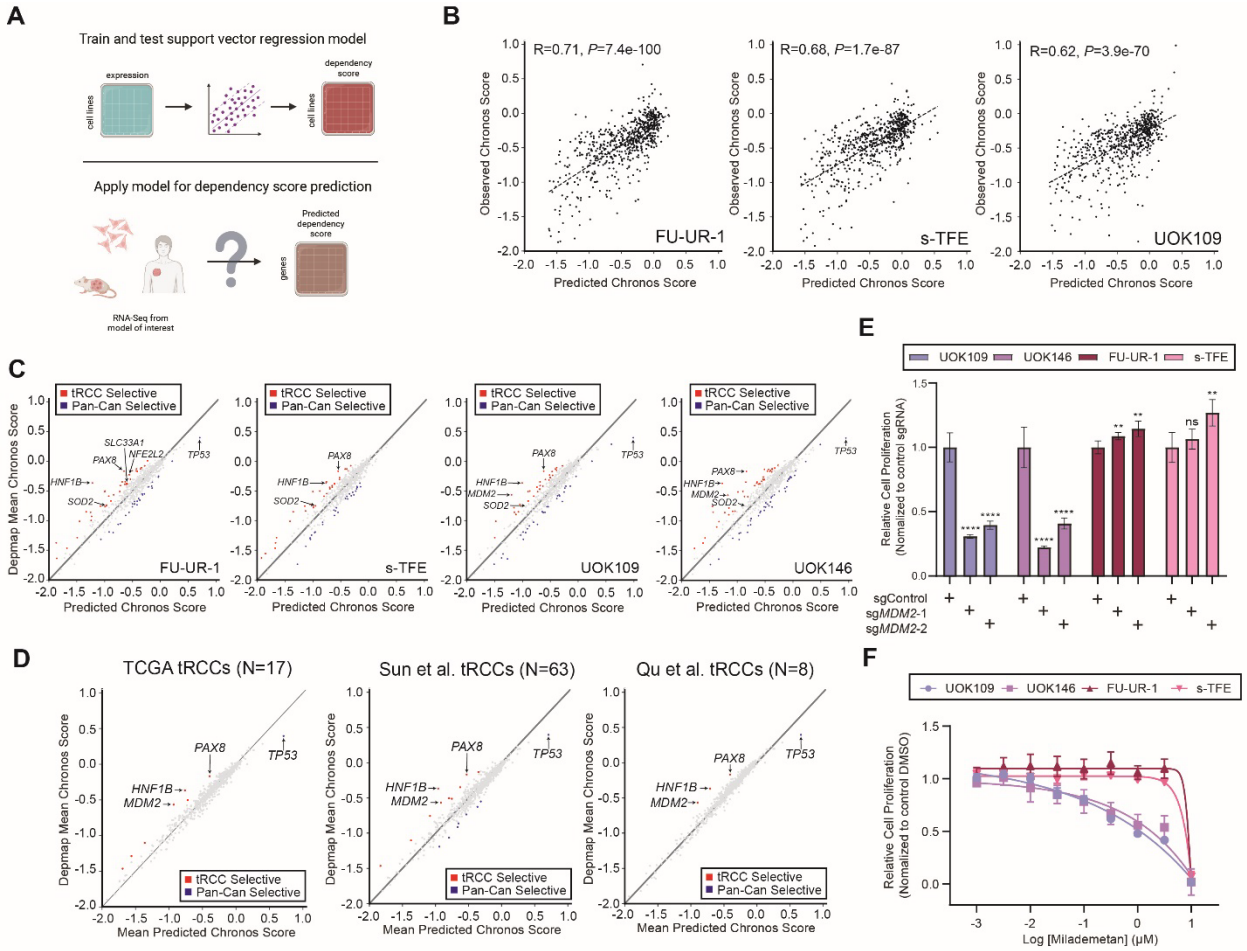

(A) Schematic of machine learning approach used to nominate candidate vulnerabilities in cell lines or tumors based on RNA-Seq profile.

(B) Correlation between observed Chronos score from CRISPR screen performed in this study and Chronos score predicted by our model, for 645 dependencies across three tRCC cell lines (FU-UR-1, S-TFE, UOK109; *Note*: discrepancy in number of genes predicted (N=657) and plotted (N=645) due to imperfect overlap in genes screened between Avana [DepMap] and Brunello libraries [tRCC screen]). *P*-values calculated from Pearson's correlation test.

(C) tRCC-selective dependencies based on predicted Chronos scores across four tRCC cell lines, including one line (UOK146) that was not assessed by genome-scale CRISPR screening. In each cell line, predicted Chronos scores in the tRCC cell line are plotted against mean Chronos score across all DepMap cell lines (as experimentally determined by genome-scale CRISPR screening). Red: ΔChronos ≤ -0.2; blue: ΔChronos ≥ 0.2 between predicted and DepMap mean.

(D) tRCC-selective dependencies based on mean predicted Chronos scores for 657 genes across tRCC tumors in three independent cohorts, as compared with mean Chronos score across all DepMap cell lines (red: ΔChronos ≤ -0.2; blue: ΔChronos ≥ 0.2 between mean predicted and DepMap mean Chronos scores).

(E) Relative viability of tRCC cells (UOK109, UOK146, FU-UR-1, s-TFE) after CRISPR/Cas9 knockout of *MDM2*. Viability is normalized to control sgRNA, shown as mean +/- s.d., n=6 biological replicates per condition. *P*-values were calculated by Welch's (two-tailed unpaired) t test as compared with sgControl samples. **P* < 0.05, ***P* < 0.01, ****P* < 0.001, *****P* < 0.0001.

(F) Viability of tRCC cell lines treated with indicated concentrations of milademetan (MDM2 inhibitor) and assayed for cell viability after 3 days with CellTiter-Glo. Viability at each concentration is relative to vehicle-treated cells, shown as mean +/- s.d., n=6 biological replicates.

984 **Fig.4 | Predicting and validating dependencies in ASPS**

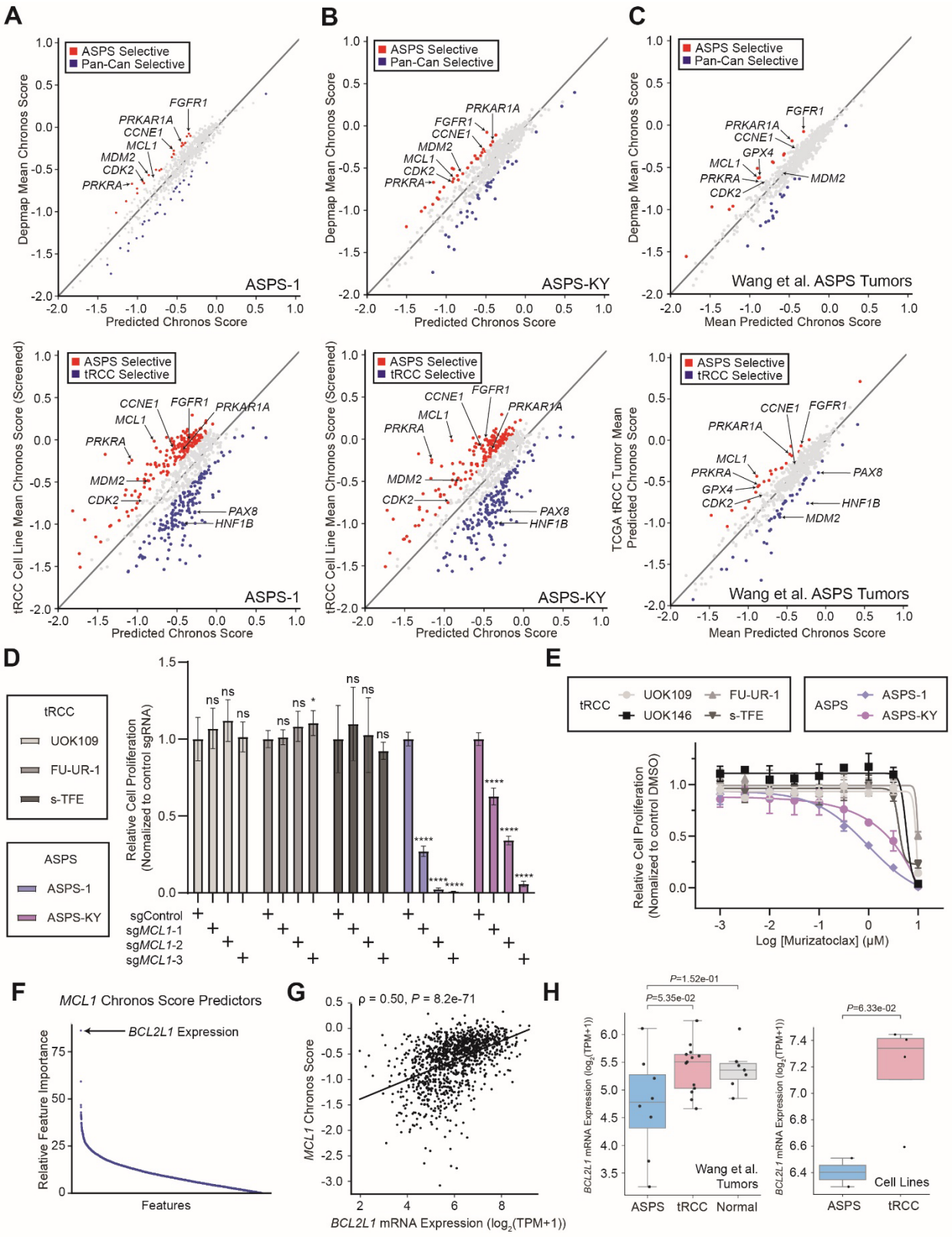

985

986

(A-C) Selective dependencies in ASPS cell lines(ASPS-1 **(A)**, ASPS-KY **(B)**) or ASPS tumors (**(C)**, profiled by RNA-Seq in a prior study (67)) based on their (mean) predicted Chronos scores as compared with mean Chronos score across all DepMap cell lines (top panels) or tRCC cell lines/TCGA tRCC tumors that were screened/predicted in this study (bottom panels). Red: ΔChronos ≤ -0.2; blue: ΔChronos ≥ 0.2 between (mean) predicted Chronos score and DepMap mean (top) or tRCC cell line/TCGA tRCC tumor mean (bottom).

(D) Proliferation of ASPS cell lines transduced with one of 3 distinct sgRNAs targeting *MCL1* or a non-targeting sgRNA control. Shown as mean +/- s.d., n = 6 biological replicates per condition. *P*-values were calculated by Welch's t-test (two-tailed unpaired) as compared with sgControl samples. **P* < 0.05, ***P* < 0.01, ****P* < 0.001, *****P* < 0.0001.

(E) Viability of ASPS-1 and ASPS-KY and non-ASPS (versus tRCC) cell lines treated with indicated concentrations of murizatoclax (MCL1 inhibitor) and assayed for cell viability after 3 days with CellTiter-Glo. Viability at each concentration is relative to vehicle-treated cells, shown as mean +/- s.d., n=3 replicates.

(F) Relative feature importance (ranked across top 5000 features) for RNA predictors of *MCL1* Chronos score. Each point represents an individual feature (see **Methods**).

(G) *MCL1* Chronos score is plotted against *BCL2L1* mRNA expression ($\log_2$(TPM+1)) across all DepMap cell lines.

(H) *BCL2L1* mRNA expression ($\log_2$(TPM+1)) in ASPS tumors, tRCC tumors, and kidney-adjacent normal tissue from Wang et al. (67) (left) as well as ASPS cell lines (ASPS-1, ASPS-KY) and tRCC cell lines (FU-UR-1, s-TFE, UOK109, UOK146) (right) profiled by RNA-seq are shown. *P*-values computed by Welch's (two-tailed unpaired) t-test.

1008 **Fig.5 | A landscape of candidate dependencies across TCGA**

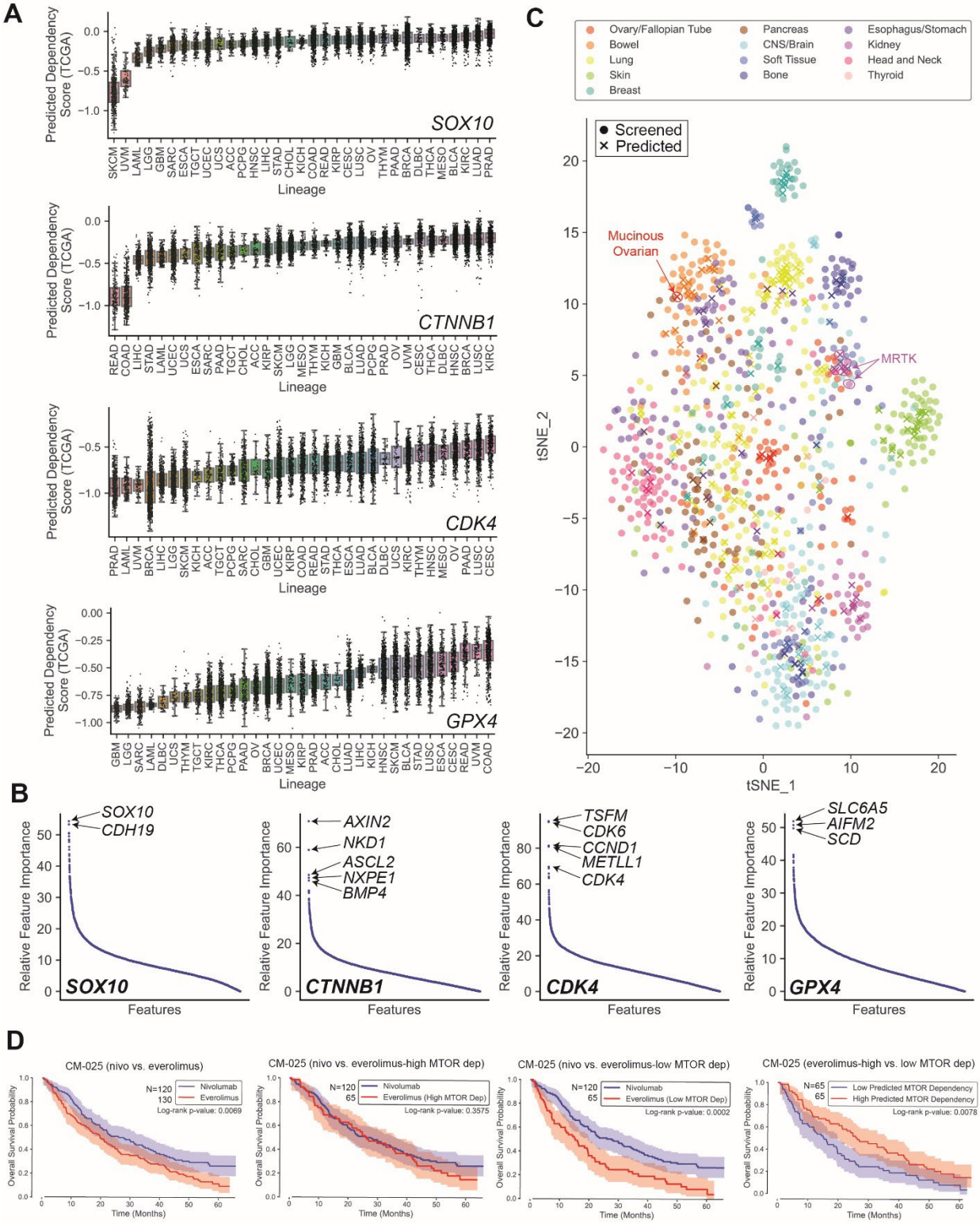

1009

1010

(A) Predicted Chronos scores for *SOX10*, *CTNNB1*, *CDK4* and *GPX*4 across tumor types profiled in TCGA; tumors grouped by TCGA lineage.

(B) Relative feature importance (ranked across top 5000 features) for RNA predictors of *SOX10*, *CTNNB1*, *CDK4* and *GPX*4 Chronos scores. Each point represents an individual feature (see **Methods**).

(C) *t*-SNE projection based on dependency score for cell lines experimentally screened in the DepMap (N=833, circle) or cell lines for which dependencies for 657 PD genes were predicted by our model (N=251 cell lines, cross). Cell lines are colored based on annotated lineage, with 13 common lineages plotted (lineages with ≥10 predicted cell lines; hematological lineages and fibroblasts removed). Selected cell lines whose dependency predictions diverge from the parental lineage are highlighted.

(D) Overall survival (OS) for ccRCC patients on clinical trial of nivolumab vs. everolimus (CM-025). From left to right: nivolumab vs. everolimus in the overall population; nivolumab vs. everolimus-treated patients with high predicted *MTOR* dependency; nivolumab vs. everolimus-treated patients with low predicted *MTOR* dependency; everolimus-treated patients with high vs. low predicted *MTOR* dependency. *P*-values calculated by log-rank test.

1026

Fig.6 | A landscape of candidate dependencies across rare kidney cancers

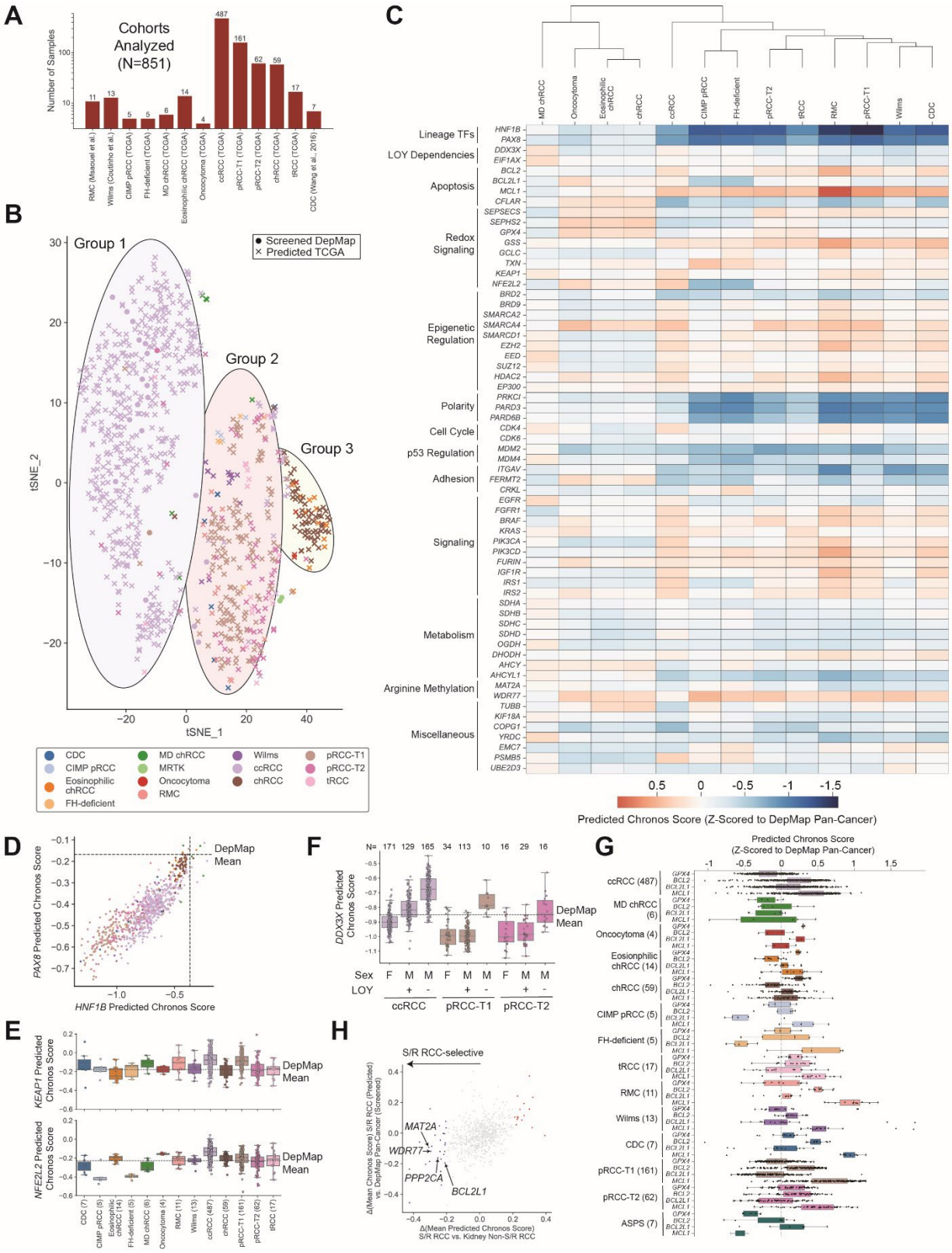

1027

1028

(A) RNA-Seq data from 851 renal tumor-derived samples was curated from across 4 published datasets (59,122–124), representing 13 distinct types of kidney cancer. The number of samples for each kidney cancer subtype is shown.

(B) *t*-SNE projection based on dependency score for kidney tumors with dependencies predicted by our model (N=851, cross) and kidney cancer cell lines experimentally screened in the DepMap (N=22), across 657 PD genes. Tumors are colored based on annotated subtype and three groups are outlined.

(C) Heatmap of predicted Chronos score (Z-scored to DepMap pan-cancer value for screened cell lines) for 63 curated dependencies, including those selective in one or more subtypes of kidney cancer (relative to pan-cancer) or additional actionable dependencies with small molecule inhibitors. Individual kidney tumor subtypes are as in **Fig.6A-B**. Hierarchical clustering is based on genes shown in the heatmap.

(D) Scatter plot of predicted *HNF1B* Chronos score versus predicted *PAX8* Chronos score for individual kidney tumors (N=851), colored by subtype as indicated in **Fig.6B**. DepMap mean Chronos score for each of these genes across experimentally screened cell lines is indicated by dotted lines.

(E) Box plot of predicted *KEAP1* (top) and *NFE2L2* (bottom) Chronos score for individual kidney tumors (N=851), grouped by subtype indicated in **Fig.6A-B**. Mean Chronos score in DepMap (experimentally derived) for these genes are indicated by dotted lines. All box plots are shown with median, upper and lower quartile lines, and extend to [Q1-1.5xIQR, Q3+1.5xIQR].

(F) Box plot of predicted *DDX3X* Chronos score across ccRCC, pRCC-T1, and pRCC-T2 tumors in TCGA stratified by annotated sex and loss of chrY (LOY) status (107). Experimentally derived mean Chronos score for *DDX3X* in DepMap is indicated as a dotted line.

(G) Box plot of predicted *GPX4*, *BCL2*, *BCL2L1*, and *MCL1* Chronos score (Z-scored to DepMap pan-cancer) for individual kidney tumors (N=851), grouped by subtype indicated in **Fig.6A**. DepMap mean (Z=0) is indicated as a dotted line. Predictions for ASPS, which was experimentally confirmed to be *MCL1* dependent (**Fig.4**) are also shown as reference.

(H) Predicted dependency scores for S/R RCCs vs. non-S/R RCCs in TCGA (94). Difference in mean predicted Chronos score between S/R RCCs and non-S/R RCCs is plotted against the difference in mean Chronos score between S/R RCCs (predicted) and the DepMap pan-cancer mean. Points are colored based on the comparison between S/R RCCs and non-S/R RCCs (blue: ΔChronos $\leq$ -0.2, $P < 0.05$; red: ΔChronos $\geq$ 0.2, $P < 0.05$ from Welch's two-tailed unpaired t-test).

Methods

Cell lines

H460 (ATCC® HTB-177; RRID:CVCL_0459), PC3 (ATCC® CRL-1435, RRID:CVCL_0035), 786-O (ATCC® CRL-1932™; RRID:CVCL_1051), 293T (ATCC® CRL-11268™; RRID:CVCL_0063), Caki-1 (ATCC® HTB-46™; RRID:CVCL_0234), UOK109 (Dr. W. Marston Linehan's laboratory, National Cancer Institute; RRID:CVCL_B087), UOK146 (Dr. W. Marston Linehan's laboratory, National Cancer Institute, RRID:CVCL_B123), s-TFE (RIKEN, #RCB4699, RRID:CVCL_R854), ASPS-1 (Dr. Robert H Shoemaker's laboratory, National Cancer Institute; RRID:CVCL_S738), and ASPS-KY (RIKEN, #RCB5683, RRID:CVCL_S737) cell lines were cultured at 37°C in DMEM with 10% FBS, 100 U/mL penicillin, and 100 µg/mL Normocin (#NC9390718). The FU-UR-1 (Dr. Masako Ishiguro's laboratory, Fukuoka University School of Medicine, RRID:CVCL_6997) cell line was cultured at 37°C in DMEM/F12 (1:1) with 10% FBS, 100 U/mL penicillin, and 100 µg/mL Normocin.

Genome-scale CRISPR knockout screens

For the UOK109, FU-UR-1, and s-TFE cell lines, Cas9-expressing cells were constructed as follows: each parental cell line was seeded in 12-well plates (2.5 × 10^5 cells/well) and incubated at 37°C overnight. The following day, the medium was replaced, and cells were incubated with lentivirus corresponding to the pLX_311-Cas9 plasmid (RRID:Addgene_96924), which encodes the Cas9 protein, and 0.8 µg/mL polybrene. After overnight incubation at 37°C, the cells were trypsinized the following day and cultured in selective media containing 5 µg/mL blasticidin. After selection, Cas9 expression and activity were confirmed in each transduced cell line via western blotting and a Cas9-activity assay as described in a previous reference (125).

The Broad Institute Brunello sgRNA library (77,441 sgRNAs targeting 19,114 genes with 1,000 non-targeting control sgRNAs) was applied for the CRISPR Screen (126,127). UOK109, FU-UR-1, and s-TFE cells were seeded into 12-well plates at a density of 1.5/1.25/1.5 x 10^6 cells/well, with 1.2 µg/mL polybrene and virus titrated at MOI <0.3 and spun at 1000 xg for 2 hours at 33°C. After spinfection, 1 mL medium was added to each well and incubated at 37°C overnight. The following day, all cells were trypsinized and expanded into 15 cm plates at 4 x 10^6 cells/plate with 4/5/5 µg/mL puromycin for a week. Medium with puromycin was replaced every 3 days. After puromycin selection, cells were seeded at 3 x 10^6 cells/plate and replated every 7 days in 15 cm plates for 21 days. At 28 days post-infection, cells were collected and stored at -20°C before genomic DNA was collected.

Genomic DNA was collected with Takara NucleoSpin Blood Kits (Macherey-Nagel), following the manufacturer's protocol. Before sequencing, genomic DNA samples were amplified by PCR.

Lentiviral production

All sgRNAs were cloned into plentiCRISPRv2 (RRID:Addgene_52961, puromycin resistance) as described (128,129). Sequence of primers for sgRNA cloning are listed in **Supplementary Table S2**. All the constructs were confirmed by Sanger sequencing.

Lentivirus was prepared by transfecting 293T cells with three plasmids: plentiCRISPRv2 (RRID:Addgene_86153), psPAX2 (RRID:Addgene_12260), and pMD2.G (RRID:Addgene_12259) using polyethylenimine (PEI). Media was replaced with standard growth media after 12 hours, and supernatant containing the virus was collected 48 hours post-transfection.

Validation of genome-scale CRISPR-Cas9 screens and dependency predictions

PC3, H460, Caki-1, 786-O, UOK109, UOK146, FU-UR-1, s-TFE, and ASPS-1 cell lines were transduced with lentivirus expressing CRISPR-Cas9 and sgRNA targeting the gene of interest, selected by puromycin, and then seeded in 96-well plates for confluence and proliferation assays with cell densities of 400-2,000 cells/well depending on the cell line. On days 7-28, depending on the cell line, cell growth medium was removed from

the plates and the Cell Titer Glo reagent (Promega, #G7571) was added following the user's instructions. Plates were then shaken at room temperature for 10 minutes. Luminescence was measured on a SpectraMax plate reader. For cell confluence assays, cell confluence on each plate was determined using a Celigo Imaging Cytometer daily.

For drug assays, cells were incubated with milademetan (MCE: #HY-101266) or murizatoclax (MCE: #HY-109184) for 3 days as indicated. Cell Titer Glo assay was measured using a SpectraMax plate reader.

Competition assay

Caki-1, 786-O, UOK109, FU-UR-1, and s-TFE were transduced with lentivirus expressing GFP, CRISPR-Cas9, and sgRNA (either control sgRNA (098) or sgRNA against TFE3). After 3 days, the GFP-positive rate was measured by a Fortessa flow cytometer to ensure it was higher than 90%. Seven days after viral infection, viral-infected cells were mixed with non-infected parental cells in a 1:1 ratio. Mixed cells were plated in 6-well plates. On days 3-24, cells were trypsinized and resuspended in 4% FACS buffer (FBS/PBS), and the GFP-positive rate was measured by a Fortessa flow cytometer. All flow cytometry data were analyzed with FlowJo (RRID:SCR_008520). GFP positive percentage in each condition at each time point was first normalized to value in that condition at d0, and then normalized to sgControl.

Colony Formation Assays

PC3, H460, Caki-1, 786-O, UOK109, UOK146, FU-UR-1, s-TFE, and ASPS-1 cell lines were transduced with lentivirus expressing CRISPR-Cas9 and sgRNA targeting the gene of interest, selected by puromycin, and then seeded in 12-well plates at various cell densities of 500-6,000 cells/well depending on the cell line. Media was replaced every 7 days. After 10-28 days, medium was aspirated, and cells were fixed and stained with 0.5% crystal violet in 25% (volume) methanol solution for about 15 minutes. Stained cells were washed with water and air-dried. Plates were scanned with an Epson scanner and quantified using ImageJ (RRID:SCR_003070).

Chronos Score Calculation

Log_2(fold-changes) in sgRNA abundance on day 28 of the screen were calculated using MAGeCK (130), using plasmid DNA as a reference. Exome sequencing data was aligned to hg38 using bwa mem (131), and copy-number was calculated using PureCN (132), as previously described (44). Chronos was used to normalize log_2(fold-changes) in sgRNAs with segmental copy-number correction (31). ccRCC cell lines were defined based on Cellosaurus NCIt disease type and included: OSRC2, CAKI2, SLR23, KMRC20, UOK101, SLR24, KMRC3, CAKI1, TUHR10TKB, SLR26, KMRC1, KMRC2 (RRID:CVCL_2984), SNU349, UMRC3, and RCCFG2.

Support Vector Regression Model

Model development and evaluation

The DepMap (RRID:SCR_017655) 23Q2 expression matrix (converted to log_2(TPM+1), https://depmap.org) and 23Q2 CRISPR-KO dependency score matrix (Chronos-normalized, https://depmap.org) were downloaded and subset to shared cell lines. We split these data into 5 equal subsets for 5-fold cross-validation (four training folds and evaluation on a validation fold). Expression was Z-scored for each gene. For each gene, a new model was trained to predict its dependency score.

To reduce dimensionality, we first calculated the Pearson correlation coefficient between each feature (i.e. Z-scored gene expression) and the dependency score of the gene being analyzed in the training data. The top predictive features for each gene (ranked by absolute value of Pearson correlation coefficient, 5000 in final model [a number that we varied to maximize performance], see **Supplementary Fig. S3B**) were determined.

For each gene, we subset the training data to these top features and trained a support vector regression model (sklearn.svm.SVR, RBF kernel) to predict dependency scores. We tested a variety of other models from sklearn including SVR with a linear kernel, ridge regression, lasso regression, elastic net, and k-nearest neighbors regression (**Supplementary Fig. S3B**). Performance on the validation fold was assessed by Pearson

correlation between predicted and observed (i.e. experimentally determined) Chronos scores for each gene across all cell lines in the validation fold. We repeated this process four more times (changing the validation fold) during cross-validation. Performance metrics were averaged between these five models for each gene. SVR with an RBF kernel had the best performance across all models tested with 657 genes being highly predictable (defined as R ≥ 0.4 between predicted and observed Chronos scores) (**Supplementary Fig. S3b**). The average Pearson correlation coefficient for predicted vs. observed Chronos score was R=0.16 across 16845 genes. The correlation between predicted and observed Chronos score across all gene-cancer cell line pairs in the test data was R = 0.92. Specifics and code for the developed pipeline as well as scripts for interactive visualization of predicted dependencies in this manuscript are available in Github: https://github.com/SViswanathanLab/TrPLet.

Model deployment

The models for each gene were retrained on the entire DepMap dataset prior to testing on external datasets. To calculate approximate coefficients from the model, we used a kernel trick taking the linear combination of support vector weighted by dual coefficients from RBF kernel. Broadly, our model was applied to three types of data: (1) TCGA tumor RNA-seq, (2) non-TCGA tumor RNA-seq, (3) cell line RNA-seq. (1) For TCGA tumor RNA-seq, we Z-scored the expression of each gene ($\log_2$(TPM+1)) within TCGA and predicted on the resulting normalized expression data. Clustering (two-component t-SNE) based on dependency scores (predicted: TCGA, experimentally-derived via CRISPR screen: DepMap) using this approach resulted in TCGA tumors clustering with screened cell lines from DepMap of the same lineage (see **Supplementary Fig. S6A**). (2) For non-TCGA tumor RNA-seq, we downloaded RNA-seq fastq files or count matrices when present, from the Gene Expression Omnibus (GEO; RRID:SCR_005012). Reads were aligned to GENCODE (RRID:SCR_014966) v38 transcript reference using STAR/RSEM (133,134). The resulting count matrices were inner joined with the TCGA count matrix (135) (https://osf.io/gqrz9/files/osfstorage), and batch corrected using ComBat-seq (136) using lineage as a covariate (for this purpose, tRCCs, Wilms' tumors, CDC, and RMC were classified as "KIRP"; ASPS, PEComa, and EHE were classified as "SARC"; ccRCC was classified as "KIRC"). The counts were then normalized to gene-level transcripts per kilobase million (TPM), converted to $\log_2$(TPM+1), and each gene's expression was then Z-scored (across the combined matrix consisting of the external dataset and TCGA). The resulting Z-scored expression in the external dataset was then used for prediction, as described above. (3) For cell line RNA-seq, a gene-level normalized expression matrix ($\log_2$(TPM+1)) was either downloaded or generated from STAR/RSEM. The expression of each gene in the resulting matrix was scaled (Z-scored) using the mean/standard deviation calculated when scaling the DepMap expression matrix. The resulting Z-scored expression values were used for prediction. Batch correction was forgone in this use-case based on tSNE clustering of tRCC cell lines with kidney cell lines in DepMap, and ASPS cell lines with soft tissue and CNS cell lines in DepMap based on expression profile (**Supplementary Fig. S6K**).

Survival Analysis

Count matrices from CM-025 (137) were used to predict MTOR dependency in ccRCC samples. Outcomes (overall survival, progression-free survival) between groups were compared using lifelines (138). Blinding, randomization not relevant to this study because analysis of these data was retrospective. Analyses were not stratified by sex as a biological variable.